
How Out-of-Equilibrium Phase Transitions can Seed Pattern Formation in Trained Diffusion Models

Luca Ambrogioni
Radboud University

Abstract

In this work, we propose a theoretical framework that interprets the generation process in trained diffusion models as an instance of out-of-equilibrium phase transitions. We argue that, rather than evolving smoothly from noise to data, reverse diffusion passes through a critical regime in which small spatial fluctuations are amplified and seed the emergence of large-scale structure. Our central insight is that architectural constraints, such as locality, sparsity, and translation equivariance, transform memorization-driven instabilities into collective spatial modes, enabling the formation of coherent patterns beyond the training data. Using analytically tractable patch score models, we show how classical symmetry-breaking bifurcations generalize into spatially extended critical phenomena described by softening Fourier modes and growing correlation lengths. We further connect these dynamics to effective field theories of the Ginzburg–Landau type and to mechanisms of pattern formation in non-equilibrium physics. Empirical results on trained convolutional diffusion models corroborate the theory, revealing signatures of criticality including mode softening and rapid growth of spatial correlations. Finally, we demonstrate that this critical regime has practical relevance: targeted perturbations, such as classifier-free guidance pulses applied at the estimated critical time, significantly improve generation control. Together, these findings position non-equilibrium critical phenomena as a unifying principle for understanding, and potentially improving, the behavior of modern diffusion models.

1 Introduction

Generative diffusion models have recently emerged as one of the most successful frameworks for high-fidelity image and video synthesis (Sohl-Dickstein et al., 2015; Ho et al., 2020; Song et al., 2021; Karras et al., 2022a). In these models, samples are generated by integrating a learned reverse diffusion process that transforms Gaussian noise into structured data. Despite their empirical success, the dynamical mechanisms by which the reverse process constructs coherent samples remain only partially understood. Recent theoretical work suggests that reverse diffusion does not simply interpolate smoothly from noise to data but instead proceeds through distinct dynamical regimes. In particular, several studies interpret the generative process in terms of phase-transition–like behavior, where the noise-symmetric state becomes unstable and trajectories begin to concentrate around modes of the data distribution (Biroli et al., 2024; Raya & Ambrogioni, 2024; Sakamoto et al., 2024; Esteban-Casadevall et al.). Complementary analyses introduce the notion of critical windows, short intervals of diffusion time during which specific features of the final sample become determined (Li & Chen, 2024; Li et al., 2025).

In statistical physics, abrupt changes in macroscopic structure are often explained through the mechanism of *spontaneous symmetry breaking* phase transitions (Landau, 1937; Kadanoff, 1966; Wilson, 1971; Wilson & Fisher, 1972; Stanley, 1971). A familiar example is the formation of magnetic order: although the microscopic laws treat all directions equally, a magnet below its critical temperature spontaneously selects a particular orientation. Small fluctuations, which would normally

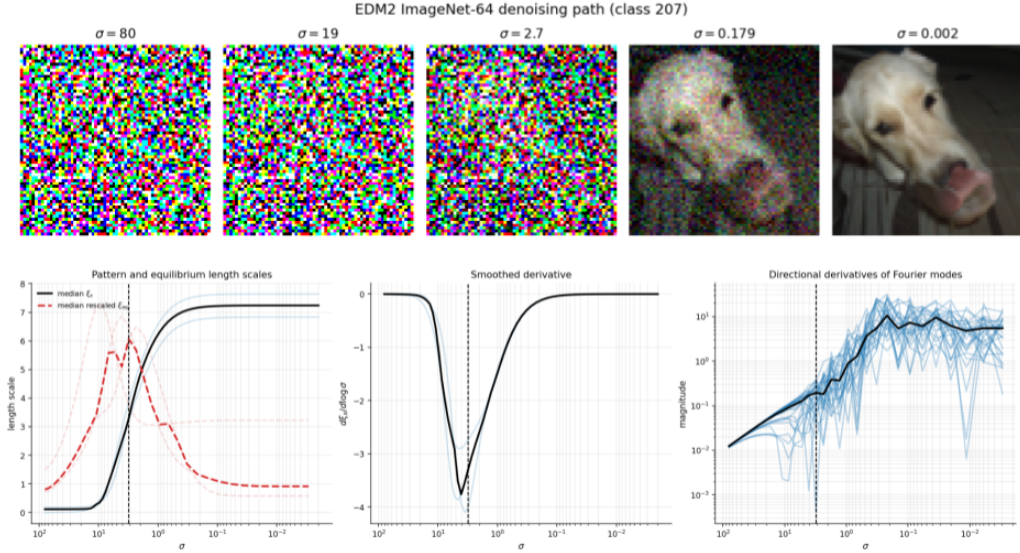


Figure 1: Quantitative analysis of pattern formation dynamics in a trained EDM2 model (Karras et al., 2022b). Top: Example generative denoised trajectory. Left: spatial correlation length $\xi_x(t)$ along several reverse trajectories (transparent blue) and their median (black). The dashed red curves show the equilibrium correlation length estimate $\xi_{\text{eq}}(t)$ obtained from the normalized low-frequency dispersion of the reverse-drift Jacobian. Middle: derivative $d\xi_x/d \log t$ highlighting the rapid growth of spatial coherence near the estimated critical time. Right: magnitude of directional derivatives along several Fourier modes (transparent) together with their median (black), showing the softening of spatial modes

remain insignificant, can become amplified near critical points and drive the system toward one of many symmetry-broken configurations. Recently, there have been efforts to directly connect sudden transitions to proper phase transitions in the statistical physics sense (Sclocchi et al., 2025b; Ambrogioni, 2025). Most notably, Sclocchi and collaborators showed that, in the denoising dynamics of specialized hierarchical diffusion models, the correlation length and dynamical susceptibility peak at a specific noise level, indicating that large regions of the sample change coherently near the transition (Sclocchi et al., 2025a). At the same time, Kamb and coauthors show that simple locality and translationally invariance assumptions lead to complex pattern formation phenomena that are highly predictive of the patterns generated by convolutional diffusion models (Kamb & Ganguli, 2025). However, a precise connection with the theory of critical phase transitions is still missing since these works involve either finite-dimensional symmetry-breaking pitchfork effects (Raya & Ambrogioni, 2024; Biroli et al., 2024) or specific hierarchical models (Sclocchi et al., 2025b,a). Furthermore, these works limit their theoretical analysis to the exact score of analytically tractable distributions and it is therefore unclear how they apply to trained networks.

In this paper, we argue that the dynamics of trained diffusion networks often exhibit symmetry breaking out-of-equilibrium crossovers that can correspond to genuine phase transitions in the thermodynamic limit. Our key insight is that the structure of these phase transitions comes from the interplay between the symmetries in the data and architectural constraints in the network architecture, which introduce locality, sparsity and invariance structure. We begin by reviewing the symmetry-breaking bifurcations introduced in (Raya & Ambrogioni, 2024), which often describe transitions between memorized datapoints or discrete classes in the empirical score. We then show that training can transform these memorization-induced bifurcations into spatially extended critical phenomena by encoding data as structured patterns of connectivity, allowing the system to generate new patterns rather than merely reproduce stored ones. Our framework builds on the analytical perspective introduced by (Kamb & Ganguli, 2025), whose locality-based formulation provides a concrete realization of the mechanisms we study.

Contributions. Our main contributions are:

- **Criticality as a mechanism for structure formation in diffusion models.** We show that the reverse diffusion process can pass through a *critical dynamical regime* where spatial correlations rapidly grow and coherent structures emerge from noise. This provides a principled explanation for the abrupt appearance of structured patterns commonly observed during denoising trajectories.
- **Architectural constraints transform memorization into collective generative dynamics.** We demonstrate that while unconstrained score models exhibit memorization-driven bifurcations tied to individual data points, architectural constraints such as *locality and translation equivariance* convert these instabilities into collective spatial modes capable of generating novel configurations.
- **Analytical and empirical evidence for critical pattern formation.** Using analytically tractable patch models, numerical simulations, and experiments on *trained convolutional diffusion networks* (see for example Fig.1), we show that reverse diffusion exhibits some of the characteristic signatures of out-of-equilibrium criticality, including softening of spatial modes followed by the emergence of large-scale patterns.
- **Guidance susceptibility.** In ImageNet experiments, we show that pulses of classifier-free-guidance (Ho & Salimans, 2022) delivered at the estimated "critical time" are more effective at aligning the generation to the class than random pulses, suggesting that the system is highly susceptible to external perturbations.

2 Background on generative diffusion

Diffusion models generate samples by learning to reverse a gradual corruption of the data distribution with Gaussian noise. Let $p_{\text{data}}(x_0)$ denote the data distribution. In the variance-preserving (VP) formulation (Song et al., 2021), the forward process follows $dx_t = -\frac{1}{2}\beta(t)x_t dt + \sqrt{\beta(t)}dW_t$, whose solution can be written $x_t = \alpha(t)x_0 + \sigma(t)\epsilon$, $\epsilon \sim \mathcal{N}(0, I)$, with $\alpha(t) = \exp\left(-\frac{1}{2}\int_0^t \beta(s) ds\right)$, $\sigma^2(t) = 1 - \alpha(t)^2$. Given data $\{x_j\}_{j=1}^N$, a score network $s_\theta(x, t)$ is trained with denoising score matching (Ho et al., 2020). The nonparametric optimum corresponds to the empirical score

$$\nabla \log \hat{p}_t(x_t) = \sum_{j=1}^N w_j(x_t) \nabla_{x_t} \log p_t(x_t^j | x_0^j), \quad (1)$$

where $w_j(x_t) = p(x_0 = x_0^j | x_t) \propto p_t(x_t | x_0^j)$ are normalized Bayesian weights. Once the score is learned, samples are generated by the reverse-time SDE

$$dx_t = \left[-\frac{1}{2}\beta(t)x_t - \beta(t)s_\theta(x_t, t) \right] dt + \sqrt{\beta(t)}d\bar{W}_t. \quad (2)$$

From a physics perspective, this is an annealed process since t has both the role of dynamic time and effective temperature of the potential. As we shall see, this is what causes out-of-equilibrium phase transitions in the generative dynamics.

3 Background on finite dimensional symmetry breaking bifurcations

We will now formalize the theory of symmetry breaking outlined in (Raya & Ambrogioni, 2024) and (Biroli et al., 2024; Achilli et al., 2026; Handke et al., 2026). For simplicity, consider a symmetric dataset consisting of two prototypes, $p_{\text{data}}(x) = \frac{1}{2}\delta(x - \mu) + \frac{1}{2}\delta(x + \mu)$, with $\mu \in \mathbb{R}^N$. After Gaussian noising with variance $\sigma^2(t)$, the forward marginal becomes a two-component Gaussian mixture whose log-density can be written as

$$\log \hat{p}_t(x) = -\frac{1}{2\sigma^2} \|x\|^2 + \log \cosh \left(\frac{\langle \mu, x \rangle}{\sigma^2} \right) + \text{const}. \quad (3)$$

The nonlinearity depends only on the global projection $\langle \mu, x \rangle$, so the empirical geometry couples all coordinates through a single collective mode. Linearizing the score at the symmetric fixed point yields the Hessian $H^* = -\frac{1}{\sigma^2}I + \frac{1}{\sigma^4}\mu\mu^\top$. Its spectrum consists of an $(N - 1)$ -fold degenerate stable

eigenvalue and a single eigenvalue along the direction of μ . The first instability occurs when this eigenvalue crosses zero, so the unstable manifold is one-dimensional. Projecting the deterministic drift component of the reverse dynamics onto this direction and defining $m = \frac{\langle \mu, x \rangle}{\|\mu\|^2}$, one obtains, to leading order, the reverse differential equation

$$\dot{m} = -g(t)^2 r(t) m - u m^3, \quad r(t) = \frac{1}{\sigma^2} - \frac{\|\mu\|^2}{\sigma^4}. \quad (4)$$

When $r(t)$ changes sign, a supercritical pitchfork bifurcation occurs with equilibria $m_{\pm} \sim \sqrt{-r(t)}$.

This instability is purely mean-field. A single eigenvalue crosses zero, the center manifold is finite-dimensional, and the order parameter scales with exponent $1/2$. The empirical Hessian is globally coupled and low-rank, so even in high dimension the instability remains collective rather than spatial. This bifurcation is formally identical to a Curie-Weiss mean field phase transition in statistical physics (Ambrogioni, 2025). Intuitively, the selection of one of the patterns is analogous to the spontaneous formation of a macroscopic field along a specific direction in a magnet at low enough temperature.

4 pattern formation through architectural constraints

The goal of this section is to understand how architectural structure constrains the symmetry-breaking mechanisms that can appear in the learned dynamics. We begin by briefly recalling the learning setup. Let $\mathcal{F} = \{s_{\theta}(\cdot, t) \mid \theta \in \Theta\}$ denote the class of score fields realizable by a given neural architecture. The parameters are learned by minimizing the denoising score-matching objective

$$\mathcal{L}(\theta) = \mathbb{E}_{t, x_0, \epsilon} \left[\|s_{\theta}(x_t, t) - \nabla_{x_t} \log p_t(x_t \mid x_0)\|^2 \right], \quad (5)$$

where $x_t = \alpha(t)x_0 + \sigma(t)\epsilon$ is the forward diffusion process. If the function class \mathcal{F} were sufficiently expressive, minimizing this loss would allow the network to recover the empirical score field associated with the dataset.

Recent work shows that the transition from memorization to generalization in diffusion models often behaves like a phase change, driven by dataset size and model capacity, where models shift from reproducing training samples to learning the underlying data distribution Halder & Pehlevan (2024); Biroli et al. (2024). This transition can also be understood through an associative memory perspective, with a critical load separating regimes Pham et al. (2025). From a dynamical standpoint, training introduces distinct timescales for generalization and memorization, creating a transient window of good generalization Bonnaire et al. (2025). Additionally, memorization is influenced by noise scale and sampling dynamics, with intermediate noise and trajectory collapse playing a key role (Dodson et al., 2026; Kim et al., 2025). Generally speaking, the transition happens when the network cannot individually represent the data points. In this paper, we study this transition in terms of the local linearized dynamics at the symmetric point, which characterizes the structure of the instabilities. In practice, neural architectures impose strong structural constraints on the vector fields that can be represented. These constraints arise from architectural features such as locality, sparsity, parameter sharing, and equivariance. The key question is whether, for large patterns, the instability directions associated with the empirical mixture model can remain isolated eigenvectors of the projected operator. In architectures with bounded receptive fields, each coordinate interacts only with a fixed-size neighborhood of radius R . The resulting Jacobian therefore contains nonzero entries only within a band determined by the receptive field. The number of independent couplings per site is $O(|\Omega|)$, where $|\Omega|$ is the number of sites in the receptive field. Consequently, the total number of free parameters in the linearized operator scales as

$$O(N|\Omega|), \quad (6)$$

rather than $O(N^2)$. Isolating a specific dense vector $v \in \mathbb{R}^N$ as an eigenvector of a matrix generically requires imposing $O(N)$ independent constraints on the operator entries. While a dense matrix with $O(N^2)$ parameters can easily satisfy such constraints, an operator with only $O(N|\Omega|)$ degrees of freedom cannot generically realize arbitrary dense projectors unless the pattern possesses special structure compatible with the local interaction geometry.

An even stronger restriction arises when the architecture is translation equivariant, as in convolutional score networks. In that case the Jacobian becomes a convolution operator,

$$(H_t x)_i = \sum_{u \in \Omega} K_t(u) x_{i+u}, \quad (7)$$

where K_t is the interaction kernel and Ω is the receptive field. Such operators are diagonalized by spatial Fourier modes. The eigenvectors of H_t are therefore $v_k(r) = e^{ikr}$. The spectrum of the operator is given by the Fourier transform of the kernel, $\lambda(k) = \sum_{u \in \Omega} K_t(u) e^{iku}$. This structure severely restricts the possible instability mechanisms. In large systems, many Fourier modes with nearby wavelengths can soften simultaneously, producing a continuum of near-degenerate unstable directions.

5 From pitchfork bifurcations to soft spatial modes and pattern formation

In the previous section, we argued that training a model can convert the individual decisions corresponding to the data points into a far richer collective process of generation, often through local interactions. Critical phase transitions happen when a continuum set of eigenvalues is suppressed at the same time, which essentially correspond to amplifications of arbitrarily rich spatial patterns from noisy fluctuations. The instability then involves many degrees of freedom rather than a single collective coordinate. As discussed above, when the system possesses approximate translation symmetry it is natural to describe perturbations in terms of spatial Fourier modes, $x(r) = \sum_k q_k e^{ikr}$, which evolve approximately as $\dot{q}_k \approx \lambda(k) q_k$, where q_k is a complex coefficient that determines the amplitude and phase of the configuration at the given frequency mode. Each mode corresponds to fluctuations at a particular spatial scale: small k represents long-wavelength variations while large k corresponds to finer structure. An instability occurs when the eigenvalues $\lambda(k)$ approach zero for a range of spatial frequencies. Modes whose eigenvalues approach zero are called *soft modes*. Near the instability the restoring force along these directions becomes small, so fluctuations at the corresponding spatial scales grow large and dominate the dynamics. In nearly equilibrated stochastic systems, susceptibility to the noise is captured by the correlation function $C_{ij}(t) = \langle x_i x_j \rangle_t - \langle x_i \rangle_t \langle x_j \rangle_t$, where the expectations are taken with respect to the equilibrium distribution associated with the score at time t . In spatially extended systems in equilibrium these correlations typically decay exponentially with distance,

$$C(r; t) \sim e^{-r/\xi(t)}, \quad (8)$$

which defines the *correlation length* $\xi(t)$. The softening of the models leads to a divergence of the equilibrium correlation length, which gives rise to long-range correlation and demarcate the critical point of a second order phase transition.

In generative diffusion, the system is out-of equilibrium, which means that the noise cannot fully propagate and cause an observable divergence of the correlation length. Instead, out-of-equilibrium systems critical instability acts as a seed for later pattern formation driven by non-linearities that act on the amplified noise fluctuations (Turing, 1952; Swift & Hohenberg, 1977). In physics, analogous dynamic phenomena are studied as examples of the Kibble–Zurek mechanism, which was developed to study domain structure formation through cosmological phase transitions in the early universe (Kibble, 1976). In this out-of-equilibrium setting, fluctuations that would normally equilibrate are instead frozen and subsequently amplified, producing coherent domains whose characteristic scale reflects the underlying critical dynamics.

6 Critical pattern formation in the patch score model

We will now analyze a tractable analytic example. Our main argument is that proper criticalities, with a corresponding critical scaling in the range of spatial correlations, emerge in diffusion models as a consequence of the limitation in the model class \mathcal{F} , which can convert the global patterns described above into local coupling structures. We will start by analyzing a simple analytic example and then move to the general theory for real neural architectures. To avoid unnecessary complexity, we will first consider the simple analytical model introduced in (Kamb & Ganguli, 2025) and a very simple dataset consisting of only two 'data points'. We will discuss the general case in later sections. Here, to capture the essence of the phenomenon, we consider the minimal Z_2 -symmetric dataset $x_0 = Y \mathbf{1}$, $Y \in \{+1, -1\}$, $\mathbb{P}(Y = \pm 1) = \frac{1}{2}$. We provide a similar analysis of the full multi-patch model from a spin glass perspective in Supp. B. In the simple case, it is easy to derive that the empirical score is: $\nabla \log \hat{p}_t(x_t) = -\frac{x}{\sigma^2(t)} + \frac{\alpha(t)}{\sigma^2(t)} \mathbb{E}[Y | X = x] \mathbf{1}$. Since the posterior expectation $\mathbb{E}[Y | X = x]$ depends on the entire configuration x , the empirical score is intrinsically nonlocal. Following (Kamb & Ganguli, 2025), we now impose a local 'architectural'

constraint. Let $\Omega \subset \mathbb{Z}^d$ be a finite receptive field containing the origin and restrict the score network to $s_i(x, t) = f_t(x_{\Omega_i})$, $x_{\Omega_i} = \{x_{i+u} : u \in \Omega\}$. where f_t is an arbitrary local function that must be optimized. Because the class depends only on x_{Ω_i} , the score-matching optimization can be performed analytically:

$$s_i(x, t) = \frac{1}{\sigma^2(t)} \left[\alpha(t) \tanh\left(\frac{\alpha(t)}{\sigma^2(t)} S_i(x)\right) - x_i \right]. \quad (9)$$

where we used the definition $S_i(x) := \sum_{u \in \Omega} x_{i+u}$. Expanding the score around the symmetric state $x = 0$ gives $\tanh z = z - \frac{z^3}{3} + O(z^5)$, so that

$$s_i(x, t) = -\frac{x_i}{\sigma^2(t)} + \frac{\alpha(t)}{\sigma^4(t)} \sum_{u \in \Omega} x_{i+u} - \frac{\alpha^2(t)}{3\sigma^8(t)} \left(\sum_{u \in \Omega} x_{i+u} \right)^3 + \dots \quad (10)$$

The linear terms are the gradient of the quadratic Hamiltonian

$$\mathcal{H}_2[x; t] = \frac{1}{2\sigma^2(t)} \sum_i x_i^2 - \frac{J_{\text{eff}}(t)}{2} \sum_i \sum_{u \in \Omega} x_i x_{i+u},$$

with $J_{\text{sym}}(t) = \frac{\alpha(t)}{\sigma^4(t)}$. The stationarity condition $s_i = 0$ yields the mean-field equation $m(t) = \alpha(t) \tanh\left(\frac{\alpha(t) |\Omega| m(t)}{\sigma^2(t)}\right)$. Expanding around this branch by writing $x_i = m(t) + \delta_i$ therefore gives a coupled dynamics with effective coupling

$$J_{\text{eff}}(t) = \frac{\alpha^2(t)}{\sigma^4(t)} \text{sech}^2\left(\frac{\alpha(t) |\Omega| m(t)}{\sigma^2(t)}\right).$$

Note that the coupling vanishes for $t \rightarrow 0$ as local statistical fluctuations are suppressed in this regime due to the rigid structure of the patches.

6.1 Long-wavelength limit, Ginzburg–Landau theory and critical scaling

We will now connect the model to the well-known Ginzburg–Landau theory (Landau, 1937; Ginzburg & Landau, 1950). The quadratic Hamiltonian derived above describes a lattice system with finite-range interactions determined by the receptive field Ω . To understand the nature of the instability it is convenient to analyze the long-wavelength limit, where the relevant fluctuations vary on spatial scales much larger than the diameter of Ω . In this regime the discrete variables x_i can be approximated by a coarse-grained field $\phi(\mathbf{r})$ defined over continuous space. Expanding the neighborhood sum around site i gives $\sum_{u \in \Omega} x_{i+u} \approx |\Omega| \phi(\mathbf{r}) + c_\Omega \nabla^2 \phi(\mathbf{r}) + O(\nabla^4)$, where c_Ω is a constant determined by the geometry of the receptive field. Substituting this expansion into the quadratic Hamiltonian yields, after coarse-graining, an effective continuum energy functional

$$\mathcal{H}[\phi; t] = \int d^d r \left[\frac{1}{2} r(t) \phi^2 + \frac{1}{2} \kappa(t) (\nabla \phi)^2 + \frac{u(t)}{4} \phi^4 \right],$$

which corresponds to the standard Ginzburg–Landau ϕ^4 field theory with Z_2 symmetry. The parameter $r(t)$ changes sign at the same point where the symmetric branch of the lattice model becomes unstable. As $r(t) \rightarrow 0^+$ the correlation length diverges, indicating the emergence of long-range spatial correlations. In the thermodynamic limit this corresponds to a continuous phase transition described by the Z_2 -symmetric ϕ^4 field theory, whose critical behavior belongs to the Ising universality class associated with finite-range interactions. Note that here Ginzburg–Landau here is not being used as an equilibrium theory, but as a local effective description of the operator content at fixed diffusion time. Equilibration would require a "freezing of the score" at the critical time, which is in principle possible but not a standard practice in generative diffusion.

6.2 Experiments on patch score model

We consider a two-dimensional patch model on a periodic 80×80 lattice. The generative model consists of 5×5 binary patches drawn from a discrete dictionary. The dictionary contains eight

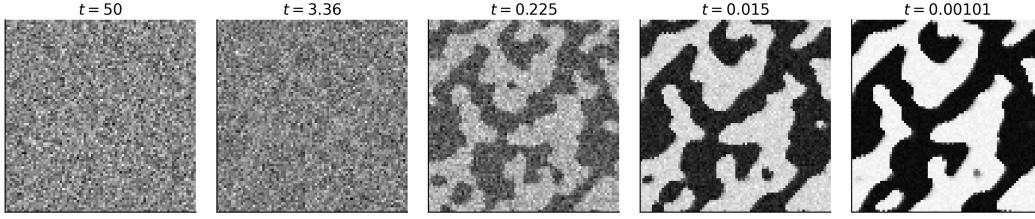


Figure 2: Five snapshots of the evolving configuration are shown at logarithmically spaced times along the reverse diffusion path.

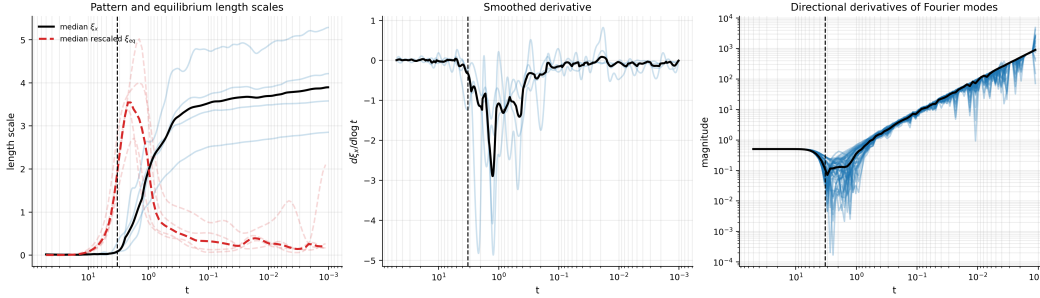


Figure 3: Quantitative analysis of pattern formation dynamics. Left: spatial correlation length $\xi_x(t)$ along several reverse trajectories (transparent blue) and their median (black). The dashed red curves show the equilibrium correlation length estimate $\xi_{eq}(t)$ obtained from the normalized low-frequency dispersion of the reverse-drift Jacobian. Middle: derivative $d\xi_x/d \log t$ highlighting the rapid growth of spatial coherence near the critical time. Right: magnitude of directional derivatives along several Fourier modes (transparent) together with their median (black), showing the softening of spatial modes near the transition.

random patterns sampled from $\{\pm 1\}^{5 \times 5}$ together with their sign-flipped copies to enforce a global \mathbb{Z}_2 symmetry. In addition, two global patterns consisting of all +1 and all -1 patches are included. The prior probability mass is concentrated on the global patterns ($p = 0.9$ total), while the eight random patterns share the remaining mass ($p = 0.1$ total). We simulate the reverse dynamics of the variance-preserving diffusion process with constant noise rate $\beta = 1$. The reverse SDE is integrated numerically on a logarithmic time grid from $T = 50$ to $t = 10^{-3}$ using 2000 integration steps. The score function $s(x, t)$ is computed analytically from the full patch posterior without linearization. Figure 2 shows the patch dictionary together with a representative reverse denoising trajectory. At early times ($t \approx T$) the system is dominated by Gaussian noise. As time decreases, local patch evidence accumulates and coherent spatial domains begin to form. Eventually the system locks into large-scale binary regions corresponding to the dominant global patterns.

To quantify the emergence of spatial structure we measure the correlation length of the binarized field

$$s(x) = \text{sign}(x) \quad (11)$$

along the reverse trajectory. The spatial correlation length $\xi_x(t)$ is estimated from the radially averaged autocorrelation function of $s(x)$. To obtain stable estimates of the temporal derivative we first smooth $\xi_x(t)$ with a Gaussian kernel before computing $d\xi_x/d \log t$. Figure 3 (left) shows $\xi_x(t)$ for several independent reverse trajectories (transparent curves) together with their median (black curve). The correlation length remains close to zero at large noise levels and increases rapidly once spatial structure begins to form. The middle panel shows the derivative $d\xi_x/d \log t$, which exhibits a pronounced peak near the onset of pattern formation. The vertical dashed line indicates the critical time

$$t_c \approx \log(26), \quad (12)$$

which corresponds to the point where spatial modes of the reverse dynamics begin to soften.

Linearized dynamics and equilibrium correlation length. To understand the origin of this transition we analyze the linearized reverse drift along the denoising trajectory. Directional derivatives

of the drift are computed along Fourier modes

$$v_k(x, y) = \cos(kx), \quad \cos(ky).$$

These directional derivatives provide estimates of the eigenvalues of the Jacobian of the reverse drift. The right panel of Fig. 3 shows the magnitude of these directional derivatives for several spatial modes. As the reverse process approaches the critical region the low-frequency modes soften simultaneously, producing a pronounced minimum near t_c . This softening signals the emergence of long-range spatial fluctuations. Using these measurements we estimate an approximate equilibrium correlation length $\xi_{\text{eq}}(t)$ associated with fluctuations around the instantaneous denoising branch. To obtain a stable estimate we consider the normalized low-frequency dispersion of the Jacobian,

$$\frac{\lambda_n(t)}{\lambda_0(t)} \approx 1 + \xi_{\text{eq}}(t)^2 (nk_{\text{min}})^2, \quad (13)$$

where $\lambda_n(t)$ denotes the directional derivative along the n -th Fourier shell and $k_{\text{min}} = 2\pi/L$. This normalization removes the rapidly increasing overall stiffness of the dynamics at small t and isolates the spatial curvature of the spectrum. Fitting this relation across the lowest Fourier shells provides an estimate of $\xi_{\text{eq}}(t)$. Note that this quantity is not a direct observable correlation due to the out-of-equilibrium nature of the dynamics, it is instead a proxy to quantify the softening of the modes at criticality. The resulting curves are shown as dashed red lines in Fig. 3. Individual trajectory estimates are shown in transparency while the median estimate is plotted in dashed red. The inferred equilibrium correlation length grows prior to the critical point, peaks close to the minimum of the soft modes, and subsequently decreases again as the dynamics locks into a stable pattern. This behavior explains why the observed pattern correlation length begins increasing before the critical time: the underlying spatial modes start softening earlier, amplifying long-wavelength fluctuations before the system fully transitions into a patterned state.

7 Out-of-Equilibrium Critical Phenomena in Real Deep Architectures

So far, we have established the existence of an out-of-equilibrium critical phenomenon within a controlled patch-based diffusion model. Importantly, this construction is not purely abstract. Patch models of this kind have been shown to reproduce, to a notable quantitative degree, the behavior of small trained convolutional diffusion networks (see (Kamb & Ganguli, 2025)). This suggests that the critical mechanism identified here captures features that can arise in learned architectures with local structure. Building on this result, we propose a broader, but necessarily conjectural, framework for realistic deep diffusion models. We do not claim to prove that modern architectures generically exhibit true critical points. Rather, we hypothesize that, depending on the symmetries of the data and the structure of the learned score Jacobian, similar instabilities may emerge in large networks. In particular, if the linearized operator develops a soft sector constrained by approximate locality and equivariance, then in a suitable large-system limit (e.g. large image size with appropriately scaled architecture), one may expect an effective description governed by the same symmetry principles as in the patch model. At a formal level, this corresponds to expanding the learned score around the relevant configuration as

$$s_{\theta,i}(x, t) = \sum_j H_{ij}(t)x_j + \frac{1}{3!} \sum_{jkl} T_{ijkl}(t)x_j x_k x_l + \dots, \quad (14)$$

where the linear operator $H_{ij}(t)$ determines the soft modes and the higher-order tensors encode the leading nonlinear interactions consistent with the symmetries. Making this precise requires a careful formulation of the “thermodynamic limit” for trained neural networks, including how architectural features scale with system size, an open and technically challenging problem. This perspective motivates a concrete empirical question: do trained diffusion models exhibit crossover regimes consistent with proximity to such critical behavior, and can these be related to underlying universality classes? Addressing this requires systematic experimental investigation on real architectures.

In fact, the results obtained on the patch model can be confirmed qualitatively on real ConvNets. We trained a model trained on the dataset FashionMNIST (Xiao et al., 2017), the details are given in Supp.F. We binarized the data so as to preserve the same approximate Ising-like symmetry group. Figure 3 shows that the results are strikingly similar to the theoretical model, with a cleared peak of equilibrium correlation length at the estimated critical point and a very sudden onset of pattern

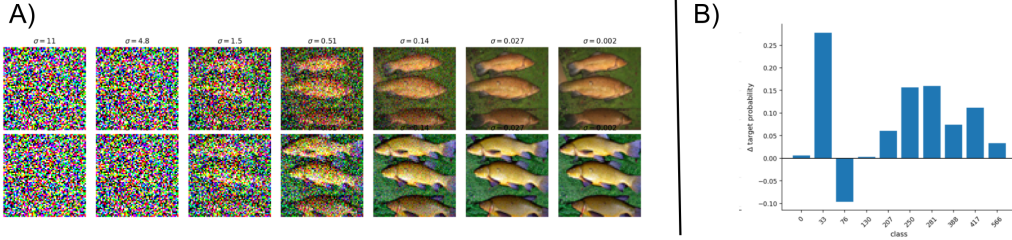


Figure 4: Results of pulse guidance experiment. A) Example image generated by the EDM2 model without critical guidance pulse (top) and with critical guidance pulse (bottom). B) Difference in class alignments (DINOv2 score) between critical pulse guidance and random pulse guidance for difference classes. Critical pulses show higher alignment for almost all tested classes.

formation starting at the estimated critical point. This qualitative agreement is significant. The patch model and the trained U-Net differ radically in their microscopic description: one is a simplified analytic system with explicit patch interactions, while the other is a high-dimensional non-linear neural network trained on real data with partial symmetries. Yet both systems exhibit the same dynamical signatures predicted by the theory, mode softening, abrupt spatial structure formation, and rapidly growing correlations. Supp. Fig 7 shows that this qualitative behavior is approximately preserved even when the model is trained on non-binarized data (under the same specifications), showing that the phenomenology is robust to changes in the symmetry structure of the data. More strikingly, as shown in Fig.1 given at the beginning of the paper, a similar phenomenology can be observed in very complex EDM2 models. In this case, the softening of the modes in less synchronized (possibly suggesting a complex pattern of phase transitions) but the inferred correlation length is clearly peaked, again, and corresponds with the onset of pattern formation. Note that the initial slope of the median mode response is due to the fact that EDM2 uses a variance exploding model, meaning that the system does not equilibrate and instead it spreads out, leading to a linear softening of all modes at high time. The EDM2 experiment is described in detail in supp.G.

Guidance pulse experiments. To test whether the critical regime identified by our dynamical analysis is functionally relevant for generation, we performed a pulse-guidance intervention on a pretrained EDM2 ImageNet diffusion model. The key idea is to apply classifier-free guidance (Ho & Salimans, 2022) only within a short window of noise scales during the reverse trajectory, rather than throughout the entire sampling process. For each class, we first estimated the reverse-diffusion dynamics and extracted the equilibrium correlation length proxy $\xi_{\text{eq}}(\sigma)$ from the normalized low-frequency dispersion of the Jacobian of the reverse drift. To reduce noise, the critical scale was not estimated separately for each class; instead, we aggregated the unguided trajectories across all classes and defined a single estimated global "critical" scale $\sigma_c = \arg \max_{\sigma} \xi_{\text{eq}}(\sigma)$. This provides an empirical estimate of the window in which long-wavelength modes are maximally softened. We then compared two intervention strategies. In the *critical-pulse* condition, a strong pulse of classifier-free guidance was applied only within a narrow interval centered at σ_c . In the *random-pulse* condition, an equally strong pulse with the same duration was applied at a random noise scale, sampled uniformly in σ . For each of 10 ImageNet classes we generated 40 samples per condition. Final samples were scored using a pretrained DINOv2 ImageNet classifier, and class alignment was quantified by the target-class logit and probability. Details are given in Supp. H. Figure 4 shows that, across classes, pulses delivered near the critical window systematically improved class alignment relative to pulses delivered at random times. This shows that the regime identified by the low-frequency softening analysis is not merely descriptive: it marks a stage of the reverse dynamics where perturbations have higher leverage over the emerging large-scale structure.

8 Conclusion

Overall, our theory and results suggest that concepts from non-equilibrium statistical physics, instabilities, soft modes, and effective field theories provide a useful organizing framework for understanding trained diffusion models. Our guidance results also demonstrate that this framework and the estimator we suggested, such as the estimated equilibrium correlation length, have potential practical values in real world applications. We highlight the need for further theoretical and empirical work to establish

this connection rigorously for more realistic models. Overall, in diffusion models, the dynamics can always be locally described by a Jacobian and there is a clear unimodal potential in the high-noise limit, making instabilities essentially unavoidable except in trivial cases (Ambrogioni, 2025; Biroli et al., 2024). What matters is not whether a true phase transition exists in the finite system, but how these instabilities organize: in finite systems, they typically appear as crossovers rather than sharp critical points. This is entirely analogous to physics, where the thermodynamic limit is a conceptual tool since real systems are finite and out of equilibrium, yet still exhibit regimes influenced by universality classes. In real models, the value of this framework is therefore methodological and diagnostic: it provides concrete tools (spectra, correlations, mode structure) to identify when diffusion dynamics enter regimes that are well described by critical-like behavior, even if only approximately.

9 Acknowledgments

The author wishes to thank the participants of the Aspen Winter Conference Theoretical Physics for Artificial Intelligence (2026) for the insightful discussions that contributed to the ideas developed in this work. In particular, the author is grateful to Mason Kamb and Akhil Premkumar.

The author also acknowledges the role of GPT-5.4 in conceptual brainstorming, experimental implementation, and collaborative drafting of this manuscript. The system served as a high-fidelity intellectual partner, assisting in refining and evaluating the underlying physical theory, as well as in implementing the experimental code. However, the final synthesis, theoretical framing, and verification of all claims remain the sole responsibility of the author.

References

- Beatrice Achilli, Marco Benedetti, Giulio Biroli, and Marc Mézard. Theory of speciation transitions in diffusion models with general class structure. *arXiv preprint arXiv:2602.04404*, 2026.
- Luca Ambrogioni. The statistical thermodynamics of generative diffusion models: Phase transitions, symmetry breaking, and critical instability. *Entropy*, 27(3):291, 2025.
- Giulio Biroli, Tony Bonnaire, Valentin de Bortoli, and Marc Mézard. Dynamical regimes of diffusion models. *Nature Communications*, 15:9957, 2024. doi: 10.1038/s41467-024-54281-3.
- Louis Bonnaire et al. Why diffusion models don’t memorize: The role of implicit dynamical regularization. In *Advances in Neural Information Processing Systems (NeurIPS)*, 2025.
- Ethan Dodson et al. Two calm ends and the wild middle: Memorization across noise scales in diffusion models. *arXiv preprint arXiv:2602.17846*, 2026.
- Maria Esteban-Casadevall, Rafal Karczewski, Alison Pouplin, Søren Hauberg, and Erik J Bekkers. On the fisher geometry of diffusion models’ latent space. In *ICLR 2026 Workshop on Geometry-grounded Representation Learning and Generative Modeling*.
- Vitaly L Ginzburg and Lev D Landau. On the theory of superconductivity. *Zhurnal Eksperimentalnoi i Teoreticheskoi Fiziki*, 20:1064–1082, 1950.
- Aritra Halder and Cengiz Pehlevan. On the onset of memorization to generalization transition in diffusion models. *arXiv preprint arXiv:2402.xxxxx*, 2024.
- Florian Handke, Dejan Stančević, Felix Koulischer, Thomas Demeester, and Luca Ambrogioni. The entropic signature of class speciation in diffusion models. *arXiv preprint arXiv:2602.09651*, 2026.
- Jonathan Ho and Tim Salimans. Classifier-free diffusion guidance. In *NeurIPS 2021 Workshop on Deep Generative Models and Downstream Applications*, 2022.
- Jonathan Ho, Ajay Jain, and Pieter Abbeel. Denoising diffusion probabilistic models. In *Advances in Neural Information Processing Systems*, volume 33, pp. 6840–6851, 2020.
- John J Hopfield. Neural networks and physical systems with emergent collective computational abilities. *Proceedings of the National Academy of Sciences*, 79(8):2554–2558, 1982. doi: 10.1073/pnas.79.8.2554.

- Leo P Kadanoff. Scaling laws for ising models near tc. *Physics Physique Fizika*, 2(6):263–272, 1966. doi: 10.1103/PhysicsPhysiqueFizika.2.263.
- Mason Kamb and Surya Ganguli. An analytic theory of creativity in convolutional diffusion models. In *Proceedings of the 42nd International Conference on Machine Learning*, volume 267 of *Proceedings of Machine Learning Research*. PMLR, 2025.
- Tero Karras, Miika Aittala, Timo Aila, and Samuli Laine. Elucidating the design space of diffusion-based generative models. In *Advances in Neural Information Processing Systems*, 2022a.
- Tero Karras, Miika Aittala, Timo Aila, and Samuli Laine. Elucidating the design space of diffusion-based generative models. *Advances in neural information processing systems*, 35:26565–26577, 2022b.
- Tom W. B. Kibble. Topology of cosmic domains and strings. *Journal of Physics A: Mathematical and General*, 9(8):1387–1398, 1976. doi: 10.1088/0305-4470/9/8/029.
- Dongjun Kim et al. How diffusion models memorize: An empirical study of trajectory collapse. *arXiv preprint arXiv:2501.xxxxx*, 2025.
- Lev D Landau. On the theory of phase transitions. *Zhurnal Eksperimentalnoi i Teoreticheskoi Fiziki*, 7:19–32, 1937.
- Marvin Li and Sitan Chen. Critical windows: Non-asymptotic theory for feature emergence in diffusion models. In *Proceedings of the 41st International Conference on Machine Learning*, volume 235 of *Proceedings of Machine Learning Research*, pp. 27474–27498, 2024.
- Marvin Li, Aayush Karan, and Sitan Chen. Blink of an eye: A simple theory for feature localization in generative models. In *Proceedings of the 42nd International Conference on Machine Learning*, volume 267 of *Proceedings of Machine Learning Research*, pp. 35047–35080, 2025.
- Trung Pham et al. Memorization to generalization: The emergence of diffusion models from associative memory. *arXiv preprint arXiv:2409.xxxxx*, 2025.
- Gabriel Raya and Luca Ambrogioni. Spontaneous symmetry breaking in generative diffusion models. *Journal of Statistical Mechanics: Theory and Experiment*, 2024(10):104025, 2024. doi: 10.1088/1742-5468/ad64bd.
- Kotaro Sakamoto, Ryosuke Sakamoto, Masato Tanabe, Masatomo Akagawa, Yusuke Hayashi, Manato Yaguchi, Masahiro Suzuki, and Yutaka Matsuo. The geometry of diffusion models: Tubular neighbourhoods and singularities. In *ICML 2024 Workshop on Geometry-grounded Representation Learning and Generative Modeling*, 2024.
- Antonio Sclocchi, Alessandro Favero, Noam Itzhak Levi, and Matthieu Wyart. Probing the latent hierarchical structure of data via diffusion models. *Journal of Statistical Mechanics: Theory and Experiment*, 2025(8):084005, 2025a. doi: 10.1088/1742-5468/ad64bd.
- Antonio Sclocchi, Alessandro Favero, and Matthieu Wyart. A phase transition in diffusion models reveals the hierarchical nature of data. *Proceedings of the National Academy of Sciences*, 122(1): e2408799121, 2025b. doi: 10.1073/pnas.2408799121.
- Jascha Sohl-Dickstein, Eric Weiss, Niru Maheswaranathan, and Surya Ganguli. Deep unsupervised learning using nonequilibrium thermodynamics. In *International Conference on Machine Learning*, pp. 2256–2265, 2015.
- Yang Song, Jascha Sohl-Dickstein, Diederik Kingma, Abhishek Kumar, Stefano Ermon, and Ben Poole. Score-based generative modeling through stochastic differential equations. In *International Conference on Learning Representations*, 2021.
- H Eugene Stanley. Phase transitions and critical phenomena. *Moscow, Mir*, 1971.
- J Swift and Pierre C Hohenberg. Hydrodynamic fluctuations at the convective instability. *Physical Review A*, 15(1):319–328, 1977. doi: 10.1103/PhysRevA.15.319.

Alan M Turing. The chemical basis of morphogenesis. *Philosophical Transactions of the Royal Society B*, 237(641):37–72, 1952. doi: 10.1098/rstb.1952.0012.

Kenneth G Wilson. Renormalization group and critical phenomena. i. renormalization group and the kadanoff scaling picture. *Physical Review B*, 4(9):3174–3183, 1971. doi: 10.1103/PhysRevB.4.3174.

Kenneth G Wilson and Michael E Fisher. Critical exponents in 3.99 dimensions. *Physical Review Letters*, 28(4):240–243, 1972. doi: 10.1103/PhysRevLett.28.240.

Han Xiao, Kashif Rasul, and Roland Vollgraf. Fashion-mnist: a novel image dataset for benchmarking machine learning algorithms. *arXiv preprint arXiv:1708.07747*, 2017.

A Explicit Ginzburg–Landau Parameters and mean-field critical time

The parameters of the coarse–grained Ginzburg–Landau (GL) description can be written explicitly in terms of the forward diffusion process and the receptive-field geometry. At tree level the coefficients are

$$r(t) = \frac{1}{\sigma^2(t)} - \frac{\alpha^2(t)}{\sigma^4(t)} |\Omega|, \quad (15)$$

$$\kappa(t) = \frac{\alpha^2(t)}{\sigma^4(t)} c_\Omega, \quad (16)$$

$$u(t) = \frac{\alpha^4(t)}{3\sigma^8(t)} |\Omega|^3. \quad (17)$$

Thus the GL parameters are completely determined by the forward diffusion statistics $(\alpha(t), \sigma(t))$ and the receptive-field geometry Ω . At the mean-field level, instability occurs when the quadratic coefficient changes sign,

$$r(t_c) = 0. \quad (18)$$

Using the expression above gives

$$\sigma^2(t_c) = \alpha^2(t_c) |\Omega|. \quad (19)$$

Since the variance-preserving process satisfies $\sigma^2(t) = 1 - \alpha^2(t)$, this yields

$$\alpha^2(t_c) = \frac{1}{1 + |\Omega|}. \quad (20)$$

For a general VP noise schedule,

$$\int_0^{t_c} \beta(s) ds = \log(1 + |\Omega|), \quad (21)$$

and for the constant schedule $\beta(t) = 1$,

$$t_c = \log(1 + |\Omega|). \quad (22)$$

This provides an explicit tree-level estimate for the time at which the long-wavelength instability underlying the critical regime appears.

B Fully random patch dictionaries and local spin-glass effective theories

In the main text we analyzed a minimal Z_2 -symmetric patch model in which the projected score induces a local ferromagnetic interaction and, in the long-wavelength limit, a Ginzburg–Landau theory of Ising type. We now consider the complementary case in which the patch dictionary is fully random. We show that, under the same locality principle, the induced effective theory is no longer ferromagnetic but instead takes the form of a finite-range disordered soft-spin model. More

precisely, the quadratic part of the frozen-time effective Hamiltonian is generated by a random local kernel of Hopfield type (Hopfield, 1982), and in regimes where its frustrated structure dominates the low-energy spectrum the corresponding dynamics is naturally described as a local spin-glass model.

The main conceptual point is that the ferromagnetic two-state model is special because the local patch covariance is rank one and aligned with the uniform mode. For a random patch ensemble, this rank-one structure is replaced by a random covariance matrix with mixed-sign fluctuations, so the projected instability is no longer associated with a single ordered magnetization mode but with a disordered family of competing local directions.

B.1 Random Z_2 symmetric patch ensemble

Let $\Omega \subset \mathbb{Z}^d$ denote the receptive field, with $|\Omega| = P$. We consider a patch dictionary

$$\mathcal{D} = \{\pm \xi^a\}_{a=1}^M, \quad \xi^a = (\xi_u^a)_{u \in \Omega}, \quad \xi_u^a \in \{\pm 1\}, \quad (23)$$

where the entries of the patterns ξ^a are sampled independently from the Rademacher distribution and then frozen. The \pm -symmetrization is essential: it guarantees an exact global Z_2 symmetry and removes any linear bias term in the expansion around the symmetric state.

At fixed diffusion time t , the corresponding local noisy patch distribution is

$$p_t^{\text{loc}}(z) = \frac{1}{2M} \sum_{a=1}^M [\mathcal{N}(z; \alpha(t)\xi^a, \sigma^2(t)I) + \mathcal{N}(z; -\alpha(t)\xi^a, \sigma^2(t)I)], \quad z \in \mathbb{R}^P. \quad (24)$$

As in the main text, the projected score field is obtained by restricting the score network to depend only on the patch variables x_{Ω_i} . The corresponding optimal local score is therefore

$$s^{\text{loc}}(z, t) = \nabla_z \log p_t^{\text{loc}}(z), \quad (25)$$

and the score at site i is obtained by evaluating the appropriate component of this local vector field on $z = x_{\Omega_i}$.

B.2 Exact form of the local score

Writing

$$h_u = \frac{\alpha(t)}{\sigma^2(t)} z_u, \quad (26)$$

the local patch density can be rewritten, up to z -independent normalization constants, as

$$p_t^{\text{loc}}(z) \propto \exp\left(-\frac{\|z\|^2}{2\sigma^2(t)}\right) \frac{1}{M} \sum_{a=1}^M \cosh(h \cdot \xi^a). \quad (27)$$

Therefore

$$\log p_t^{\text{loc}}(z) = -\frac{\|z\|^2}{2\sigma^2(t)} + \log \left[\frac{1}{M} \sum_{a=1}^M \cosh(h \cdot \xi^a) \right] + \text{const.} \quad (28)$$

Differentiating gives the exact projected local score

$$s_u^{\text{loc}}(z, t) = -\frac{z_u}{\sigma^2(t)} + \frac{\alpha(t)}{\sigma^2(t)} \frac{\sum_{a=1}^M \xi_u^a \sinh(h \cdot \xi^a)}{\sum_{a=1}^M \cosh(h \cdot \xi^a)}. \quad (29)$$

This expression is the natural multi-pattern generalization of the tanh-response obtained in the two-state model. In that special case the dictionary contains only one direction, so the posterior average collapses to a scalar hyperbolic tangent. For a random dictionary, the posterior response is instead a random nonlinear function of all patch coordinates.

B.3 Expansion around the symmetric state

To identify the effective instability structure we expand the local score around $z = 0$. Because the dictionary is exactly \pm -symmetric, odd disorder moments vanish. Hence the expansion of $\log p_t^{\text{loc}}(z)$ starts at quadratic order in z , and the score expansion begins with a linear term.

Define the empirical patch covariance matrix

$$C_{uv} = \frac{1}{M} \sum_{a=1}^M \xi_u^a \xi_v^a, \quad u, v \in \Omega. \quad (30)$$

Using $\cosh y = 1 + y^2/2 + y^4/4! + O(y^6)$, one obtains

$$\log \left[\frac{1}{M} \sum_{a=1}^M \cosh(h \cdot \xi^a) \right] = \frac{1}{2} h^\top C h + \frac{1}{4!} \kappa_4(h) + O(\|h\|^6), \quad (31)$$

where κ_4 denotes the fourth cumulant contribution generated by the random patch ensemble. Substituting $h = \alpha(t)z/\sigma^2(t)$ yields

$$\log p_t^{\text{loc}}(z) = -\frac{\|z\|^2}{2\sigma^2(t)} + \frac{\alpha^2(t)}{2\sigma^4(t)} z^\top C z + \frac{\alpha^4(t)}{4! \sigma^8(t)} \kappa_4(z) + O(\|z\|^6). \quad (32)$$

Differentiating gives

$$s_u^{\text{loc}}(z, t) = -\frac{z_u}{\sigma^2(t)} + \frac{\alpha^2(t)}{\sigma^4(t)} \sum_{v \in \Omega} C_{uv} z_v + \frac{\alpha^4(t)}{3! \sigma^8(t)} \sum_{v, w, q \in \Omega} K_{uvwq} z_v z_w z_q + O(\|z\|^5), \quad (33)$$

where K_{uvwq} is the fourth-cumulant tensor.

At this stage the analogy with the ferromagnetic patch model is immediate. In the two-state case the covariance C is proportional to the rank-one projector onto the uniform patch direction, which yields a positive local interaction. Here C is instead a random Gram matrix. The linearized projected score is therefore controlled by a random local operator rather than by a single ordered mode. This is the basic mechanism behind the emergence of a glassy effective theory.

B.4 Induced quadratic Hamiltonian

The linear term in the score is the gradient of the quadratic effective Hamiltonian

$$H_2^{\text{loc}}[z; t] = \frac{1}{2\sigma^2(t)} \sum_{u \in \Omega} z_u^2 - \frac{\alpha^2(t)}{2\sigma^4(t)} \sum_{u, v \in \Omega} C_{uv} z_u z_v. \quad (34)$$

Lifting this patch-level interaction to the full lattice in the same way as in the main text gives

$$H_2[x; t] = \frac{1}{2\sigma^2(t)} \sum_i x_i^2 - \frac{\alpha^2(t)}{2\sigma^4(t)} \sum_i \sum_{u, v \in \Omega} C_{uv} x_{i+u} x_{i+v}. \quad (35)$$

Equivalently, separating the diagonal and off-diagonal contributions,

$$H_2[x; t] = \frac{1}{2} \tilde{r}(t) \sum_i x_i^2 - \frac{1}{2} \sum_i \sum_{\substack{u, v \in \Omega \\ u \neq v}} J_{uv}(t) x_{i+u} x_{i+v}, \quad (36)$$

with

$$\tilde{r}(t) = \frac{1}{\sigma^2(t)} - \frac{\alpha^2(t)}{\sigma^4(t)}, \quad J_{uv}(t) = \frac{\alpha^2(t)}{\sigma^4(t)} C_{uv}. \quad (37)$$

This is the central result. The effective couplings are local, since they only connect variables within a common receptive field, but they are also random, because they are determined by the frozen random dictionary. Since the off-diagonal entries of C take both signs, the interactions are generically frustrated.

The disorder statistics are immediate:

$$\mathbb{E}[C_{uv}] = \delta_{uv}, \quad (38)$$

and

$$\text{Var}(C_{uv}) = \begin{cases} 0, & u = v, \\ 1/M, & u \neq v. \end{cases} \quad (39)$$

Hence, for $u \neq v$,

$$\mathbb{E}[J_{uv}(t)] = 0, \quad \text{Var}(J_{uv}(t)) = \frac{\alpha^4(t)}{\sigma^8(t)} \frac{1}{M}. \quad (40)$$

Thus the induced quadratic theory is a finite-range soft-spin model with quenched random couplings of mixed sign.

B.5 Relation to Hopfield and Edwards–Anderson spin glasses

The effective interaction kernel obtained above has the form of a finite-range Hopfield matrix built from random patch patterns. Indeed, the covariance

$$C_{uv} = \frac{1}{M} \sum_{a=1}^M \xi_u^a \xi_v^a \quad (41)$$

is precisely a local Hebbian kernel associated with the patch dictionary. Because the patterns are random and unstructured, this kernel is frustrated rather than ferromagnetic, and its low-energy behavior is naturally glassy.

It is important, however, to formulate the precise statement carefully. If the same random dictionary is used at every lattice location, then the random couplings depend on offsets inside the receptive field but do not vary explicitly from site to site. In that case the most precise characterization is as a finite-range Hopfield-type soft-spin glass kernel. By contrast, the standard Edwards–Anderson model has spatially varying random bonds. An Edwards–Anderson description arises only after additional coarse-graining or in variants of the model where the effective local pattern content fluctuates from region to region, thereby inducing site-dependent couplings $J_{i;uv}$.

Accordingly, the correct conclusion is not that the projected theory is literally the Edwards–Anderson model in all cases, but rather that it belongs to the broader class of local disordered spin-glass effective theories, with the frozen patch dictionary generating a finite-range Hopfield-type kernel as its most direct realization.

B.6 Spectral criterion for the instability

In the ferromagnetic two-state model the instability is controlled by a scalar mass parameter and occurs when the corresponding coefficient changes sign. In the random patch model the criterion is instead spectral. At the patch level, the quadratic form becomes unstable when the largest eigenvalue of the random covariance matrix overcomes the local restoring term:

$$\frac{1}{\sigma^2(t_c)} = \frac{\alpha^2(t_c)}{\sigma^4(t_c)} \lambda_{\max}(C). \quad (42)$$

Equivalently,

$$\sigma^2(t_c) = \alpha^2(t_c) \lambda_{\max}(C). \quad (43)$$

This should be compared with the rank-one two-state result, in which $\lambda_{\max}(C) = |\Omega|$ and the instability is carried entirely by the uniform patch mode. In the random case $\lambda_{\max}(C)$ is a disorder-dependent quantity and the unstable directions are generally not aligned with the uniform mode. The instability therefore produces a disordered soft sector rather than a clean ferromagnetic ordering channel.

This distinction is fundamental. In the two-state model the symmetry-broken phase is organized by one collective order parameter. In the random patch model the soft modes arise from a random local spectrum, and the relevant landscape contains many competing directions and metastable configurations.

B.7 Quartic stabilization and the soft-spin nature of the model

The quartic and higher-order terms in the effective theory arise from the higher cumulants of the random patch ensemble. At quartic order one obtains

$$H_4[x; t] \sim \frac{\alpha^4(t)}{\sigma^8(t)} \sum_i \sum_{u,v,w,q \in \Omega} U_{uvwq} x_{i+u} x_{i+v} x_{i+w} x_{i+q}, \quad (44)$$

for a disorder-dependent tensor U_{uvwq} . These nonlinear terms play the same formal role as in the ferromagnetic Ginzburg–Landau theory: they stabilize the dynamics once the quadratic operator develops soft or unstable directions. The crucial difference is that here the quartic tensor is itself random and anisotropic.

The proper effective theory is therefore not a clean ϕ^4 model but a random quartic soft-spin theory. This is another important technical point. The microscopic variables of diffusion are continuous, so the natural effective model is a soft-spin glass rather than a strict Ising-spin system. Only in late-time saturated regimes, or after explicit thresholding, does one recover a binary-spin description.

B.8 Quenched versus annealed disorder

A subtle but important issue concerns the order of averaging. If the random dictionary is averaged over before the effective theory is analyzed, then

$$\mathbb{E}[C] = I, \quad (45)$$

so the off-diagonal frustrated structure disappears. The quadratic score then reduces, on average, to a purely local mass renormalization with no glassy interaction channel. This annealed treatment misses the relevant physics.

The correct procedure is therefore the quenched one:

1. sample the random dictionary;
2. derive the projected local score and the induced quadratic kernel for that realization;
3. analyze the corresponding soft modes, metastable structure, and observables;
4. only then average the resulting observables over disorder realizations if desired.

This is entirely analogous to the standard treatment of spin glasses, where frustration and metastability are properties of each frozen disorder realization and are destroyed by averaging too early.

B.9 Nonequilibrium character of the reverse dynamics

The reverse diffusion process is not an equilibrium dynamics at fixed Hamiltonian but a nonstationary stochastic process whose drift changes with diffusion time. The random patch model therefore does not define a single static spin glass; rather, it defines a time-dependent family of local soft-spin-glass Hamiltonians

$$H[x; t] = H_2[x; t] + H_4[x; t] + \dots \quad (46)$$

through which the reverse trajectory evolves.

This distinction matters because glassy systems can have very slow relaxation. Even if the instantaneous frozen-time Hamiltonian has a glassy structure, the actual reverse trajectory may not equilibrate on the corresponding landscape before the score has changed appreciably. Thus the observable phenomenology depends on the competition between the local relaxation time and the score-evolution time scale. In the disordered case this issue is even sharper, since relaxation may be dominated by activated motion across metastable barriers.

For this reason, it is safest to describe the fully random patch model as entering a glassy regime or a local spin-glass effective regime along the reverse trajectory, rather than immediately asserting the presence of an equilibrium thermodynamic spin-glass phase.

B.10 Dimensional caveat

A further technical subtlety concerns spatial dimension. The induced couplings are finite range. For short-range spin glasses, whether a genuine thermodynamic glass transition exists depends strongly on dimension. In particular, for $d = 2$ one should be cautious about claiming a sharp finite-temperature Edwards–Anderson phase, whereas in higher dimensions such a phase is more plausible. This caveat does not weaken the central conceptual conclusion. The point of the analysis is not primarily to establish a specific equilibrium universality class, but to show how the architectural constraints of a random patch mixture naturally converts the score geometry into a local frustrated interaction structure.

B.11 Summary

The fully random Z_2 -symmetric patch model provides the disordered counterpart of the ferromagnetic patch model analyzed in the main text. Under the same locality principle, the induced local score admits an expansion

$$s_u^{\text{loc}}(z, t) = -\frac{z_u}{\sigma^2(t)} + \frac{\alpha^2(t)}{\sigma^4(t)} \sum_{v \in \Omega} C_{uv} z_v + O(\|z\|^3), \quad (47)$$

where C is the empirical covariance of the random patch dictionary. The corresponding quadratic effective Hamiltonian is

$$H_2[x; t] = \frac{1}{2} \tilde{r}(t) \sum_i x_i^2 - \frac{1}{2} \sum_i \sum_{\substack{u, v \in \Omega \\ u \neq v}} J_{uv}(t) x_{i+u} x_{i+v}, \quad J_{uv}(t) = \frac{\alpha^2(t)}{\sigma^4(t)} C_{uv}. \quad (48)$$

Because the couplings are finite range, quenched, and frustrated, the frozen-time theory is a local soft-spin glass of Hopfield type, with Edwards–Anderson-type behavior emerging after suitable coarse-graining or spatial disordering of the effective couplings. The instability is no longer tied to the uniform mode but to the top of a random local spectrum, and the resulting soft regime is controlled by disorder, frustration, and metastability rather than by ferromagnetic ordering.

In this sense, the two patch models discussed in the paper represent two opposite ends of the same mechanism: the structured two-state dictionary yields a local ferromagnet and an Ising-like critical regime, while the fully random dictionary yields a local spin-glass effective theory and a corresponding glassy regime along the reverse diffusion dynamics.

C General local architectures near criticality and spin-glass effective theories

Here we formulate the same mechanism in a more general way for arbitrary local and translation-equivariant architectures, such as convolutional score networks, and show that near criticality their behavior is controlled by a small number of soft modes. In the generic case, these soft modes are coupled through frustrated effective interactions, leading to a local soft-spin-glass description.

The key point is that near a critical point one does not need a full microscopic description of the network. Instead, the dynamics is determined by the linearized operator restricted to the soft sector together with the leading symmetry-allowed nonlinearities. This makes it possible to derive a general effective theory that is nontrivial but still controlled by locality, symmetry, and the structure imposed by training.

C.1 Local architectures and projected linear operators

Let $x = (x_i)_{i \in \Lambda}$ denote the degrees of freedom on a lattice $\Lambda \subset \mathbb{Z}^d$, and let

$$s_\theta(x, t) = (s_{\theta, i}(x, t))_{i \in \Lambda}$$

denote a trained score field at diffusion time t . We assume that the architecture satisfies the following structural conditions.

1. **Locality.** There exists a finite receptive-field radius R such that $s_{\theta, i}(x, t)$ depends only on variables x_j with $|j - i| \leq R$.

2. **Translation equivariance.** For any lattice translation τ_a ,

$$s_\theta(\tau_a x, t) = \tau_a s_\theta(x, t).$$

3. **Z_2 symmetry near the relevant branch.** Around the symmetric state,

$$s_\theta(-x, t) = -s_\theta(x, t),$$

so that $x = 0$ is a symmetric fixed point.

These assumptions are the natural generalization of the local patch setting analyzed explicitly in the main text. Near $x = 0$, the score admits the odd expansion

$$s_{\theta,i}(x, t) = \sum_j H_{ij}(t)x_j + \frac{1}{3!} \sum_{jkl} T_{ijkl}(t)x_j x_k x_l + O(\|x\|^5),$$

where $T_{ijkl}(t)$ is the cubic response tensor. By locality, both H_{ij} and T_{ijkl} have finite spatial range. The linearized reverse drift is therefore governed by a finite-range operator, in agreement with the main text's statement that local architectures convert the mean-field instability of the empirical score into the spectral softening of a local operator.

C.2 Criticality and reduction to the soft sector

Assume that at some diffusion time t_c the symmetric branch loses stability. In the notation of the main text, the transition occurs when the relevant eigenvalue of the projected linearization crosses zero. Equivalently,

$$\lambda_{\min}(H(t_c)) = 0.$$

Near t_c , only the modes whose eigenvalues are small contribute appreciably to the long-time dynamics. All other modes remain massive and can be integrated out.

Let \mathcal{S} denote the soft subspace spanned by these near-zero modes, and let $P_{\mathcal{S}}$ be the projector onto \mathcal{S} . Decompose the configuration as

$$x = \phi + \psi, \quad \phi = P_{\mathcal{S}}x, \quad \psi = (1 - P_{\mathcal{S}})x.$$

The field ψ relaxes rapidly and can be expressed perturbatively in terms of ϕ . Substituting this into the full dynamics yields an effective evolution on the soft manifold alone. Thus near criticality the reverse dynamics reduces to a stochastic field theory for a small set of slowly varying amplitudes.

This is the general version of the mechanism exhibited explicitly by the patch models in the main text. In the two-state patch model the soft sector is effectively one-dimensional and yields a ferromagnetic Z_2 -symmetric ϕ^4 theory. In the random patch model the soft sector is multi-directional and disordered, producing a glassy effective theory. The same dichotomy persists for arbitrary local architectures.

C.3 Symmetry-constrained effective theory near criticality

Because the microscopic score field is local and odd under $x \mapsto -x$, the effective theory on the soft sector must be local and Z_2 -even. Retaining terms up to quartic order in the soft amplitudes and second order in gradients, the most general effective functional has the form

$$\mathcal{F}_{\text{eff}}[\phi] = \int d^d r \left[\frac{1}{2} \sum_{ab} \phi_a M_{ab} \phi_b + \frac{1}{2} \sum_{ab, \mu\nu} \partial_\mu \phi_a K_{ab}^{\mu\nu} \partial_\nu \phi_b + \frac{1}{4!} \sum_{abcd} U_{abcd} \phi_a \phi_b \phi_c \phi_d \right] + \dots$$

Here a, b, c, d index the soft modes, M_{ab} is the mass matrix, $K_{ab}^{\mu\nu}$ is the stiffness tensor, and U_{abcd} is the quartic interaction tensor. Higher-order terms and higher gradients are omitted since they are subleading near criticality in the same sense discussed in the main text for anisotropic and higher-order nonlinearities.

If the soft sector is one-dimensional and aligned with a single ordering direction, then the theory reduces to the scalar form

$$\mathcal{F}_{\text{eff}}[\phi] = \int d^d r \left[\frac{1}{2} r(t) \phi^2 + \frac{1}{2} \kappa(t) (\nabla \phi)^2 + \frac{u(t)}{4} \phi^4 \right],$$

which is exactly the Ginzburg–Landau description obtained in the ferromagnetic patch model.

For a generic trained architecture, however, there is no reason for the soft sector to collapse to a single mode. The projected Hessian generally contains several competing directions. The mass, stiffness, and quartic tensors are then generically non-diagonal and frustrated. In that case the correct near-critical description is multicomponent and disordered.

C.4 Why generic local architectures lead to frustration

The origin of frustration is not the architecture by itself but the combination of heterogeneous data geometry and architectural constraints. The empirical score of a finite dataset is a mixture field. Its linearization around the symmetric state reflects the covariance structure of the noisy dataset and therefore contains many competing directions. The main text shows that local architectures suppress the global rank-one mode and retain only the part of this structure compatible with locality. What remains is a finite-range operator whose coefficients are determined by the data through training.

For a highly structured dataset, such as the two-state patch model, the projected covariance is rank one and positive, so all local variables align. For a generic heterogeneous dataset, the projected covariance is instead spread across several local feature directions. The resulting soft sector is characterized by:

- several near-degenerate soft modes rather than one dominant order parameter;
- couplings in the soft manifold that are not all simultaneously diagonalizable;
- quartic interactions that are anisotropic and generically sign-indefinite across mode combinations.

This is precisely the effective signature of frustration. There is, in general, no single global pattern that optimizes all couplings at once. The system instead organizes around a rough low-energy landscape with many competing local arrangements.

C.5 Local soft-spin-glass reduction

Choose a basis $\{\varphi^a(r)\}_{a=1}^m$ for the soft sector and expand

$$\phi(r) = \sum_{a=1}^m q_a(r) \varphi^a(r),$$

where $q_a(r)$ are slow amplitudes. Substituting into the effective functional yields

$$\mathcal{F}_{\text{eff}}[q] = \int d^d r \left[\frac{1}{2} \sum_{ab} q_a \mathcal{M}_{ab} q_b + \frac{1}{2} \sum_{ab, \mu\nu} \partial_\mu q_a \mathcal{K}_{ab}^{\mu\nu} \partial_\nu q_b + \frac{1}{4!} \sum_{abcd} \mathcal{U}_{abcd} q_a q_b q_c q_d \right].$$

There are now two qualitatively distinct possibilities.

Clean ordering case. If one soft mode dominates and all tensors align with it, then the above functional reduces effectively to a scalar Z_2 -symmetric ϕ^4 theory, corresponding to a local ferromagnetic critical point.

Generic disordered case. If several soft modes remain nearly degenerate and their couplings are frustrated, then the matrices \mathcal{M} , \mathcal{K} , and the quartic tensor \mathcal{U} define a multicomponent disordered soft-spin theory. In that case the natural effective description is

$$\mathcal{F}_{\text{SG}}[q] = \int d^d r \left[\frac{1}{2} \sum_{ab} q_a \mathcal{M}_{ab} q_b + \frac{1}{2} \sum_{ab, \mu\nu} \partial_\mu q_a \mathcal{K}_{ab}^{\mu\nu} \partial_\nu q_b + \frac{1}{4!} \sum_{abcd} \mathcal{U}_{abcd} q_a q_b q_c q_d \right],$$

where frustration resides in the sign and incompatibility structure of the couplings. This is the general soft-spin-glass reduction of a local architecture near criticality.

It is important to stress that the “spins” here are amplitudes of soft architectural modes, not literal Ising variables. The effective theory is therefore naturally a *soft-spin glass*, and only in strongly saturated late-time regimes or after thresholding does one recover a binary-spin description.

C.6 Translational invariance and the meaning of glassiness

A technical subtlety is that a strictly translation-equivariant architecture with fixed weights yields a translation-equivariant Jacobian. In the infinite-system limit, such an operator is diagonal in Fourier space and does not itself generate explicit bond disorder in physical space. In that strict sense the resulting theory is not automatically the Edwards–Anderson model.

Nevertheless, glassiness still arises in the effective soft sector. The frustration can live in *mode space* rather than directly in position space. Exact translation invariance is compatible with:

- several nearly degenerate soft branches,
- incompatible quartic couplings between them,
- a rugged effective landscape on the soft-mode amplitudes.

Accordingly, in the exact translation-equivariant limit the appropriate description is a *frustrated multicomponent soft-spin theory*, or equivalently a mode-space spin glass. If one then incorporates finite-size effects, weak inhomogeneities, imperfect training, boundary effects, or slow spatial variation in effective feature activation, the coefficients in the soft theory acquire weak spatial dependence,

$$\mathcal{M}_{ab} \rightarrow \mathcal{M}_{ab}(r), \quad \mathcal{U}_{abcd} \rightarrow \mathcal{U}_{abcd}(r),$$

and the theory crosses over to a genuine local soft-spin glass with effective quenched disorder in space.

Thus the most careful statement is the following. Exact translation-equivariant local architectures lead near criticality to a frustrated multicomponent soft-spin theory, while realistic finite systems generically realize its spatially disordered soft-spin-glass counterpart.

C.7 Nonequilibrium character of the glassy critical regime

As emphasized in the main text, the reverse diffusion process is not an equilibrium dynamics with fixed couplings but a nonstationary stochastic evolution whose drift changes with diffusion time. The local effective theory therefore depends on t ,

$$\mathcal{F}_{\text{eff}}[\phi; t],$$

and the system moves through a family of critical or near-critical free-energy landscapes along the reverse trajectory.

This distinction is especially important in the frustrated case. Glassy systems relax slowly, often through activated exploration of metastable states. As the critical point is approached, the relaxation time of the soft sector grows, while the score itself continues to evolve. Therefore the system need not equilibrate on the instantaneous landscape. The correct physical picture is not a static equilibrium spin glass, but a *time-dependent glassy critical regime* in which frustration, metastability, and slow soft modes compete with the time variation of the drift. This is the disordered analogue of the critical slowing-down and freeze-out mechanism discussed in the main text.

C.8 Summary

For arbitrary local and translation-equivariant architectures, the picture developed in the main text implies that the learned linearization near the symmetric state is a local operator obtained by projecting the empirical score geometry onto the realizable model class. Near a critical point, only a small set of soft modes survives. Integrating out the massive modes yields a local effective theory whose coefficients are determined by the projected Hessian and the leading symmetry-allowed nonlinearities.

If the soft sector is effectively one-dimensional and aligned with a single pattern direction, the resulting theory is the familiar local ferromagnetic Z_2 -symmetric ϕ^4 theory. In the generic case, however, the soft sector contains several competing directions and the induced couplings are frustrated. The appropriate near-critical description is then a multicomponent local soft-spin-glass theory. This provides the general architectural counterpart of the random patch model: locality enforces a small set of relevant couplings, while heterogeneous data geometry generically renders those couplings disordered and frustrated.

D Global couplings induced by attention and their spin-glass interpretation

The preceding section assumed a strictly local architecture with bounded receptive field. This assumption is essential for the suppression of the global rank-one channel emphasized in the main text. Architectures with attention modify this conclusion because they can induce couplings between distant degrees of freedom. The purpose of this section is to show how those global couplings fit naturally into the same effective-theory framework and how they can be interpreted from the perspective of spin-glass theory.

D.1 Attention as a dynamical nonlocal operator

At a fixed layer and diffusion time, a self-attention block computes outputs of the schematic form

$$y_i = \sum_j A_{ij}(x, t) V_j(x, t),$$

where $A_{ij}(x, t)$ is the attention kernel and $V_j(x, t)$ is the value representation. Even if the underlying parameters are translation equivariant, the operator induced by attention is generally nonlocal because A_{ij} couples site i to all sites j . After linearization around the symmetric state $x = 0$, one obtains an effective contribution to the score Jacobian of the form

$$H_{ij}^{\text{att}}(t),$$

which is in general dense rather than finite range.

From our viewpoint, attention therefore enlarges the realizable operator class from local sparse kernels to operators containing a nonlocal component. Instead of

$$H_t = K_t^{\text{loc}}[H_t^*],$$

one now has schematically

$$H_t = K_t^{\text{loc}}[H_t^*] + K_t^{\text{att}}[H_t^*],$$

where the first term is finite range and the second is nonlocal. The resulting instability can then contain both local and global channels.

D.2 Decomposition into local and global sectors

A useful way to organize the effect of attention is to decompose the learned Jacobian into

$$H(t) = H^{\text{loc}}(t) + H^{\text{glob}}(t),$$

where H^{loc} is the bounded-range component induced by convolutional or local interactions and H^{glob} is the dense low-rank or long-range component induced by attention. Near criticality, the effective quadratic Hamiltonian then takes the form

$$H_2[x; t] = \frac{1}{2} \sum_{ij} x_i A_{ij}(t) x_j, \quad A(t) = A^{\text{loc}}(t) + A^{\text{glob}}(t).$$

The local part gives the spatial critical behavior discussed in the main text. The global part reintroduces mean-field-like coupling channels that are otherwise suppressed in purely local architectures. Depending on its structure, A^{glob} can have several qualitatively different effects:

1. it can restore a low-rank global ordering mode, producing a mixed local/mean-field instability;
2. it can couple several distant soft modes coherently, leading to collective mode competition;
3. if the induced global couplings are sign-indefinite, it can generate a long-range frustrated interaction structure.

This last case is the natural point of contact with spin-glass theory.

D.3 Attention-induced couplings as Hopfield-type interactions

In many cases the nonlocal component induced by attention is effectively low rank. Linearizing the query-key structure around the symmetric state yields kernels of the schematic form

$$A_{ij}^{\text{glob}}(t) \approx \sum_{\alpha=1}^p \gamma_{\alpha}(t) u_i^{(\alpha)} u_j^{(\alpha)},$$

where the vectors $u^{(\alpha)}$ encode global feature directions selected by the attention mechanism. This is formally analogous to a Hopfield coupling matrix. If the global feature directions are coherent and aligned, the effect is mean-field ferromagnetic. If several competing feature directions are present with mixed signs, the effective low-rank kernel is frustrated and the corresponding frozen-time theory is a *long-range soft-spin glass of Hopfield type*.

Thus attention naturally implements a form of associative-memory coupling at the level of the effective operator. The distinction between structured generation and glassy competition is again determined by the geometry of the projected global modes:

- one dominant global mode gives a Curie–Weiss-like channel;
- many competing low-rank global modes give a Hopfield-like glassy sector.

This is precisely the nonlocal analogue of the distinction between the structured and random patch models.

D.4 Mixed local–global glassy criticality

Once both local and attention-induced terms are present, the natural effective theory near criticality is neither purely local nor purely mean-field. Instead one obtains a mixed functional of the form

$$\mathcal{F}[q] = \int d^d r \left[\frac{1}{2} \sum_{ab} q_a \mathcal{M}_{ab} q_b + \frac{1}{2} \sum_{ab, \mu\nu} \partial_{\mu} q_a \mathcal{K}_{ab}^{\mu\nu} \partial_{\nu} q_b \right] - \frac{1}{2} \sum_{ab} J_{ab}^{\text{glob}} Q_a Q_b + \frac{1}{4!} \sum_{abcd} \mathcal{U}_{abcd} q_a q_b q_c q_d + \dots,$$

where

$$Q_a = \int d^d r q_a(r)$$

is the global amplitude of soft mode a . The matrix J_{ab}^{glob} encodes the attention-induced long-range couplings. This form makes the physical structure transparent:

- the gradient term comes from local architectural couplings and controls spatial criticality;
- the global quadratic term comes from attention and couples spatially separated regions;
- the quartic tensor stabilizes the dynamics and encodes competition between channels.

If J^{glob} is positive and low rank, the model exhibits local criticality dressed by global ordering tendencies. If J^{glob} is frustrated, the resulting theory is a *mixed local–global soft-spin glass*, combining spatial domain formation with long-range mode competition. This is the natural effective description of architectures that combine convolution and attention.

D.5 Physical interpretation

From the spin-glass viewpoint, attention plays the role of adding a nonlocal interaction sector to the otherwise local projected score geometry. Convolutional structure generates finite-range couplings and therefore favors spatial criticality. Attention adds dense interactions between distant degrees of freedom and can therefore reintroduce mean-field behavior, associative-memory-like retrieval, or long-range frustration depending on the sign and rank structure of the induced kernel.

This perspective suggests a useful interpretation of hybrid diffusion architectures. Local convolutions organize fluctuations into spatially coherent domains; attention coordinates or competes between those domains at large distance. Near criticality, the interaction between these two sectors can generate rich behavior: local pattern formation, global coherence, metastable retrieval of global templates, or glassy competition among several nonlocal organizing directions.

D.6 Summary

Attention enlarges the realizable operator class by adding dense nonlocal couplings to the local projected score operator. In the effective theory, this corresponds to supplementing the local soft-spin functional by a long-range quadratic sector. When the induced global couplings are coherent, attention restores a mean-field ordering channel. When they are low-rank but frustrated, attention generates a Hopfield-type long-range glassy sector. Combined with local couplings, this yields a mixed local–global soft-spin-glass theory, which provides a natural framework for understanding hybrid convnet-attention architectures near criticality.

E Supplementary Methods: Patch Model Experiments

This section describes in detail the numerical experiments used to study the emergence of spatial structure in the reverse dynamics of the patch diffusion model. All procedures described here correspond directly to the code used to generate the figures in the main text.

E.1 Patch dictionary

The generative model is defined using a discrete dictionary of binary 5×5 patches. Each patch takes values in $\{-1, 1\}^{5 \times 5}$.

The dictionary contains:

- Eight random patterns $p_k \in \{-1, 1\}^{5 \times 5}$.
- Their sign-flipped counterparts $-p_k$ to enforce a global \mathbb{Z}_2 symmetry.
- Two uniform patterns consisting of all +1 and all –1 entries.

The resulting dictionary therefore contains ten patterns.

The prior probability distribution over patches is defined as

$$\pi_k = \begin{cases} \frac{0.1}{8}, & k = 1, \dots, 8 \\ \frac{0.9}{2}, & k = 9, 10. \end{cases} \quad (49)$$

Thus the random patches collectively carry probability 0.1 while the two uniform patterns together carry probability 0.9.

This bias toward uniform patches ensures that the global patterns represent the dominant modes of the model.

E.2 Spatial domain

The model is defined on a two–dimensional periodic lattice

$$x \in \mathbb{R}^{L \times L}$$

with

$$L = 80.$$

Periodic boundary conditions are used when extracting patch neighborhoods and computing spatial correlations.

E.3 Forward diffusion process

The forward diffusion process follows the variance-preserving stochastic differential equation

$$dx_t = -\frac{1}{2}x_t dt + dW_t. \quad (50)$$

The corresponding marginal distribution satisfies

$$x_t = \alpha(t)x_0 + \sigma(t)\varepsilon, \quad (51)$$

where

$$\alpha(t) = e^{-t/2} \quad (52)$$

$$\sigma(t) = \sqrt{1 - e^{-t}}. \quad (53)$$

E.4 Exact patch score

The score function is computed analytically from the patch dictionary. For each spatial location (i, j) we consider the 5×5 neighborhood centered at that location.

Let

$$y_{ij}$$

denote the patch extracted from the current state x_t .

The posterior probability of patch p_k is

$$w_k(i, j) \propto \pi_k \exp\left(\frac{\alpha(t)}{\sigma(t)^2} \langle p_k, y_{ij} \rangle\right). \quad (54)$$

After normalization,

$$\sum_k w_k(i, j) = 1. \quad (55)$$

The posterior mean of the central pixel of the patch is

$$m_{ij} = \sum_k w_k(i, j) p_k(0, 0). \quad (56)$$

The analytic score is then

$$s(x_t, t) = \frac{\alpha(t)m - x_t}{\sigma(t)^2}. \quad (57)$$

E.5 Reverse diffusion dynamics

The reverse SDE is

$$dx_t = \left(-\frac{1}{2}x_t - s(x_t, t)\right) dt + d\bar{W}_t. \quad (58)$$

Integration proceeds backward in time from

$$T = 50$$

to

$$t_{\min} = 10^{-3}.$$

A logarithmic time grid with 2000 steps is used:

$$t_k = \exp \left(\log T + \frac{k}{N} (\log t_{\min} - \log T) \right). \quad (59)$$

The SDE is discretized using the Euler–Maruyama scheme

$$x_{k+1} = x_k + b(x_k, t_k) \Delta t + \sqrt{|\Delta t|} \eta_k, \quad (60)$$

where

$$b(x, t) = -\frac{1}{2}x - s(x, t).$$

E.6 Pattern correlation length

Spatial structure is quantified using the correlation length of the binarized field

$$s(x) = \text{sign}(x). \quad (61)$$

The spatial autocorrelation function is computed via FFT:

$$C(r) = \frac{1}{N} \sum_{|i-j|=r} s_i s_j. \quad (62)$$

A radial average is then computed to obtain $C(r)$ as a function of distance.

The correlation length is estimated as the first moment of the positive portion of the correlation function:

$$\xi_x = \frac{\sum_r r C(r)}{\sum_r C(r)}. \quad (63)$$

E.7 Temporal derivative

To stabilize the estimate of

$$\frac{d\xi_x}{d \log t}$$

the correlation length trajectory is smoothed using a Gaussian kernel before differentiation.

E.8 Linearized dynamics

To analyze the stability of spatial modes we estimate directional derivatives of the reverse drift

$$J(x, t) = \frac{\partial b(x, t)}{\partial x}.$$

For a direction v the directional derivative is approximated using symmetric finite differences

$$\lambda_v = \frac{v^\top [b(x + \varepsilon v, t) - b(x - \varepsilon v, t)]}{2\varepsilon}. \quad (64)$$

The finite difference step is chosen adaptively as

$$\varepsilon = \max(5 \times 10^{-5}, 10^{-3} \sigma(t)^2).$$

E.9 Fourier modes

Directional derivatives are computed along Fourier modes

$$v_{n,x}(i, j) = \cos(nk_{\min}i) \quad (65)$$

$$v_{n,y}(i, j) = \cos(nk_{\min}j) \quad (66)$$

with

$$k_{\min} = \frac{2\pi}{L}.$$

Modes up to shell $n = 6$ are evaluated.

E.10 Equilibrium correlation length

To estimate the equilibrium correlation length of fluctuations around the denoising branch we analyze the low-frequency dispersion of the Jacobian.

Let

$$\lambda_n(t)$$

denote the directional derivative for shell n .

To remove the rapidly increasing stiffness of the dynamics at small t , the spectrum is normalized by the constant mode:

$$\tilde{\lambda}_n(t) = \frac{\lambda_n(t)}{\lambda_0(t)}. \quad (67)$$

For small wavenumbers the dispersion is expected to follow

$$\tilde{\lambda}_n(t) \approx 1 + \xi_{\text{eq}}(t)^2 (nk_{\min})^2. \quad (68)$$

The equilibrium correlation length is therefore estimated by fitting

$$\tilde{\lambda}_n(t) - 1 = \xi_{\text{eq}}(t)^2 (nk_{\min})^2 \quad (69)$$

over the lowest Fourier shells $n = 1, 2, 3$.

E.11 Trajectory statistics

All quantities are computed for multiple independent reverse diffusion trajectories.

For visualization:

- Individual trajectories are plotted with transparency.
- Median curves are plotted in black.
- Equilibrium correlation lengths are rescaled to match the vertical range of $\xi_x(t)$ for visualization purposes.

E.12 Critical time

The theoretical critical time of the model is

$$t_c \approx \log(26). \quad (70)$$

This time corresponds to the point where the lowest spatial modes of the linearized dynamics become maximally soft. In all figures this point is indicated by a vertical dashed line.

E.13 Summary of parameters

Grid size	80×80
Patch size	5×5
Random patches	8
Uniform patches	2
Reverse time range	$T = 50$ to 10^{-3}
Integration steps	2000
Trajectories	4
Fourier shells	$n \leq 6$

All experiments reported in the paper can be reproduced using these parameters.

F Supplementary Experiments: Trained Convolutional Diffusion Models

This section describes in detail the experimental setup used to analyze pattern formation in trained diffusion models. The goal of these experiments is to reproduce, in a trained neural network, the dynamical phenomena observed in the analytic patch model. In particular, we measure the evolution of spatial correlations, the softening of Fourier modes of the reverse drift, and the effective equilibrium correlation length along the reverse diffusion trajectory.

F.1 Dataset and preprocessing

The experiments use the Fashion-MNIST dataset, which consists of grayscale images of clothing items with spatial resolution

$$28 \times 28.$$

To simplify the statistical structure of the data and emphasize spatial pattern formation, we use a binarized version of the dataset. Each pixel is converted to a binary variable using a deterministic threshold:

$$x_{ij} = \begin{cases} +1 & \text{if } p_{ij} > 0.5, \\ -1 & \text{otherwise,} \end{cases}$$

where p_{ij} denotes the normalized grayscale pixel value.

After binarization the images satisfy

$$x \in \{-1, 1\}^{28 \times 28}.$$

This preprocessing step removes grayscale variability that is unrelated to spatial organization and makes the dataset closer to a lattice spin system, which simplifies the interpretation of the correlation analysis.

F.2 Diffusion process

We train the model using the variance-preserving (VP) diffusion formulation introduced in Section 3 of the main text. The forward diffusion process satisfies the stochastic differential equation

$$dx_t = -\frac{1}{2}x_t dt + dW_t,$$

corresponding to the constant noise schedule

$$\beta(t) = 1.$$

The solution of this process can be written in closed form as

$$x_t = \alpha(t)x_0 + \sigma(t)\varepsilon, \quad \varepsilon \sim \mathcal{N}(0, I),$$

with

$$\alpha(t) = e^{-t/2}, \quad \sigma^2(t) = 1 - e^{-t}.$$

These functions determine the statistics of the noisy data distribution used during score-matching training.

The reverse-time diffusion process is given by

$$dx_t = \left(-\frac{1}{2}x_t - s_\theta(x_t, t) \right) dt + d\bar{W}_t,$$

where $s_\theta(x, t)$ denotes the learned score function.

F.3 Network architecture

The score network is implemented as a lightweight convolutional U-Net designed for small images. The network predicts the noise field $\varepsilon_\theta(x_t, t)$ used in the standard noise-prediction formulation of diffusion models.

F.3.1 Time embedding

The diffusion time t is encoded using sinusoidal embeddings

$$\phi_k(t) = \begin{cases} \sin(\omega_k t), \\ \cos(\omega_k t), \end{cases}$$

with logarithmically spaced frequencies

$$\omega_k = \exp\left(-\frac{k}{d} \log 10000\right).$$

The embedding dimension is $d = 128$. The embedding vector is processed by a two-layer multilayer perceptron with SiLU activation.

F.3.2 Convolutional backbone

The main architecture follows an encoder–decoder structure with residual blocks.

Input layer The input image

$$x_t \in \mathbb{R}^{1 \times 28 \times 28}$$

is first processed by a 3×3 convolution producing 64 channels.

Encoder The encoder consists of two resolution stages:

- Stage 1:
 - Residual block (64 channels)
 - Strided convolution downsampling (factor 2)
- Stage 2:
 - Residual block (64 → 128 channels)
 - Strided convolution downsampling

Residual block Each residual block consists of

- Group normalization
- SiLU activation
- 3×3 convolution
- addition of projected time embedding
- Group normalization
- SiLU activation
- 3×3 convolution

If the input and output channel dimensions differ, a 1×1 convolution is used in the residual connection.

Bottleneck The bottleneck consists of two residual blocks operating at 128 channels.

Decoder The decoder mirrors the encoder structure:

- Upsampling layer
- Concatenation with skip connection
- Residual block

Two such stages are used to restore the original spatial resolution.

Output layer The final layer consists of

- Group normalization
- SiLU activation
- 3×3 convolution producing a single output channel

The network predicts the noise field $\varepsilon_\theta(x_t, t)$. The score is recovered as

$$s_\theta(x_t, t) = -\frac{\varepsilon_\theta(x_t, t)}{\sigma(t)}.$$

F.4 Training procedure

The network is trained using denoising score matching with the standard noise prediction loss

$$L(\theta) = \mathbb{E} [\|\varepsilon - \varepsilon_\theta(x_t, t)\|^2].$$

Training parameters:

Dataset	Fashion-MNIST (binarized)
Epochs	30
Batch size	256
Optimizer	AdamW
Learning rate	2×10^{-4}
Gradient clipping	1.0
Time sampling	log-uniform

Log-uniform sampling over diffusion time ensures sufficient coverage of the small-noise regime, where the reverse dynamics becomes stiff.

F.5 Reverse diffusion sampling

Samples are generated by numerically integrating the reverse SDE on a logarithmic time grid

$$t_k = \exp\left(\log T + \frac{k}{N}(\log t_{\min} - \log T)\right),$$

with parameters

$$T = 50, \quad t_{\min} = 10^{-3}, \quad N = 2000.$$

The Euler–Maruyama scheme is used for integration.

F.6 Spatial correlation analysis

To analyze spatial pattern formation we measure the correlation length of the binarized configuration

$$s(x) = \text{sign}(x).$$

The spatial correlation function is computed as

$$C(r; t) = \langle s_i s_j \rangle_{|i-j|=r}.$$

The correlation length is estimated using the first moment

$$\xi_x(t) = \frac{\sum_r r C(r)}{\sum_r C(r)}.$$

To stabilize the derivative, the correlation-length trajectory is smoothed with a Gaussian kernel before computing

$$\frac{d\xi_x}{d \log t}.$$

F.7 Linearized drift analysis

To probe the stability of spatial modes we measure directional derivatives of the reverse drift

$$b(x, t) = -\frac{1}{2}x - s_\theta(x, t).$$

For a perturbation direction v we estimate

$$\lambda_v = \frac{v^\top (b(x + \epsilon v, t) - b(x - \epsilon v, t))}{2\epsilon}.$$

This quantity approximates the eigenvalues of the Jacobian of the reverse drift.

F.8 Fourier modes

Directional derivatives are computed along spatial Fourier modes

$$v_{n,x}(i, j) = \cos(nk_{\min}i), \quad v_{n,y}(i, j) = \cos(nk_{\min}j),$$

where

$$k_{\min} = \frac{2\pi}{L}.$$

F.9 Equilibrium correlation length

Following the analysis of the patch model we estimate an equilibrium correlation length from the normalized dispersion relation

$$\frac{\lambda_n(t)}{\lambda_0(t)} \approx 1 + \xi_{\text{eq}}(t)^2 (nk_{\min})^2.$$

Fitting this relation over the lowest Fourier shells provides an estimate of $\xi_{\text{eq}}(t)$.

F.10 Trajectory statistics

All observables are computed across several independent reverse trajectories.

Plots show

- individual trajectories (transparent curves),
- the median trajectory (solid curve).

This representation highlights the robustness of the observed dynamical features.

F.11 Interpretation

The convolutional architecture imposes locality on the learned score field. As discussed in the theoretical analysis, this architectural constraint suppresses the global mean-field instability of the empirical score and replaces it with a spatial instability governed by a local operator.

As a result, the reverse diffusion dynamics exhibit:

- softening of long-wavelength modes,
- growth of spatial correlations,
- rapid emergence of coherent structure during generation.

These observations are consistent with the interpretation of diffusion generation as a nonequilibrium dynamical phase transition.

G Supplementary Experiments: Analysis of a Trained EDM2 Diffusion Model

To test whether the theoretical predictions developed in this work extend to realistic large-scale diffusion models, we analyze the reverse diffusion dynamics of a pretrained pixel-space diffusion model trained on ImageNet. The critical line is estimated empirically as the peak of the inferred correlation length. In contrast to the analytic patch model and the small convolutional experiments described in the main text, this model operates on natural images and is trained on a large dataset using a modern diffusion architecture.

Our goal is to determine whether the same phenomenology observed in the analytic model and in small trained networks also appears in a state-of-the-art generative model. In particular, we investigate whether the reverse diffusion trajectory exhibits the signatures predicted by the statistical-physics theory:

- softening of low-frequency spatial modes,
- growth of spatial correlation length during denoising,
- emergence of a critical window where correlations are maximal.

G.1 Model

We use a pretrained pixel-space diffusion model from the EDM2 framework. The model is trained on the ImageNet dataset at a spatial resolution of 64×64 pixels. The architecture is a large convolutional U-Net with attention layers and class conditioning.

The model predicts the denoised image $D_\theta(x, \sigma, y)$, where x is the current noisy image, σ is the noise level, and y is the class label. The reverse-time dynamics of the sampler can be written as

$$\frac{dx}{d\sigma} = b_\sigma(x, \sigma)$$

with drift field

$$b_\sigma(x, \sigma) = \frac{x - D_\theta(x, \sigma, y)}{\sigma}.$$

The variable σ therefore plays the role of the control parameter along the generation trajectory, replacing the diffusion time t used in the variance-preserving formulation discussed in the main text.

G.2 Reverse diffusion trajectories

Reverse diffusion trajectories are generated using the deterministic EDM sampler with Heun correction. The sampler integrates the reverse dynamics from a large initial noise level

$$\sigma_{\max} = 80$$

down to

$$\sigma_{\min} = 0.002.$$

The noise schedule is parameterized by

$$\sigma_i = \left(\sigma_{\max}^{1/\rho} + \frac{i}{N-1} (\sigma_{\min}^{1/\rho} - \sigma_{\max}^{1/\rho}) \right)^\rho$$

with $\rho = 7$. This schedule concentrates integration steps near the low-noise regime where the dynamics becomes stiff.

For each trajectory we record the intermediate images $x(\sigma_i)$ along the reverse diffusion path.

G.3 Continuous spatial correlation length

In the analytic patch model and the binarized MNIST experiments, spatial correlations were measured using a sign-binarized field. For natural images this estimator is too coarse, as it discards most amplitude information and artificially introduces sharp domain boundaries.

Instead we compute the correlation length from a continuous scalar image field.

First, RGB images are converted to luminance

$$\ell(x) = 0.2989R + 0.5870G + 0.1140B.$$

The spatial mean is subtracted to obtain a centered field

$$\tilde{\ell}(x) = \ell(x) - \langle \ell(x) \rangle.$$

The connected spatial correlation function is then computed as

$$C(r; \sigma) = \langle \tilde{\ell}(x) \tilde{\ell}(x+r) \rangle.$$

The spatial correlation length is estimated using the second-moment estimator

$$\xi_x(\sigma) = \sqrt{\frac{\sum_r r^2 C(r; \sigma)}{\sum_r C(r; \sigma)}}.$$

This estimator captures the characteristic spatial scale of image structure and evolves smoothly as large-scale organization emerges during denoising.

G.4 Linearized drift operator

To probe the stability of spatial modes we analyze the Jacobian of the reverse drift field

$$b_\sigma(x, \sigma) = \frac{x - D_\theta(x, \sigma, y)}{\sigma}.$$

Directional derivatives of the Jacobian are computed using finite differences. For a perturbation direction v we estimate

$$\lambda_v(\sigma) = \frac{v^\top [b_\sigma(x + \epsilon v, \sigma) - b_\sigma(x - \epsilon v, \sigma)]}{2\epsilon}.$$

This quantity approximates the curvature of the drift operator along the direction v .

G.5 Fourier-mode analysis

To analyze spatial instabilities we evaluate directional derivatives along Fourier modes

$$v_{n,x}(i, j) = \cos(nk_{\min} i), \quad v_{n,y}(i, j) = \cos(nk_{\min} j)$$

with

$$k_{\min} = \frac{2\pi}{L}$$

where L is the image size.

These directions probe the stability of spatial modes with increasing wavelength. The resulting quantities $\lambda_n(\sigma)$ approximate the dispersion relation of the linearized operator.

G.6 Equilibrium correlation length estimator

Following the analysis developed for the analytic model, we estimate an equilibrium correlation length from the normalized dispersion relation

$$\frac{\lambda_n(\sigma)}{\lambda_0(\sigma)} \approx 1 + \xi_{\text{eq}}(\sigma)^2 (nk_{\min})^2.$$

This normalization removes the overall stiffness of the dynamics and isolates the curvature of the spatial spectrum near $k = 0$.

The estimator is obtained by fitting the low-frequency modes of the dispersion relation.

G.7 Empirical critical scale

Unlike the analytic patch model, the trained neural network does not admit a closed-form expression for the coefficient $r(\sigma)$ of the effective Ginzburg–Landau theory. Consequently the critical point cannot be determined analytically.

Instead we define an empirical critical scale σ_c as the value of σ where the estimated equilibrium correlation length reaches its maximum:

$$\sigma_c = \arg \max_{\sigma} \xi_{\text{eq}}(\sigma).$$

In the theoretical description this corresponds to the point where the quadratic coefficient $r(\sigma)$ of the effective field theory approaches zero, indicating that the lowest spatial modes become maximally soft.

G.8 Trajectory statistics

All observables are computed across multiple independent reverse diffusion trajectories.

Plots display:

- individual trajectories as transparent curves,
- the median trajectory as a solid curve.

This visualization highlights the consistency of the dynamical features across samples.

G.9 Interpretation

The results show that the reverse diffusion dynamics of a large pretrained ImageNet model exhibit the same qualitative behavior predicted by the statistical–physics framework. As the noise level decreases, long-wavelength spatial modes soften and the spatial correlation length grows, indicating the emergence of coherent structure across the image.

The correlation length reaches a maximum within a narrow window of noise levels before decreasing again as the system enters a rigid low-noise regime. This behavior is consistent with the nonequilibrium critical dynamics described in the main text, where the reverse diffusion trajectory passes through a rounded critical regime during which spatial correlations are amplified before the system settles into a stable configuration.

H Supplementary Methods: Guidance pulse experiments in a pretrained EDM2 model

This section describes the guidance pulse experiments performed on a pretrained EDM2 ImageNet diffusion model. The objective of these experiments is to test whether the critical regime identified by the dynamical analysis of the reverse process also corresponds to a window of enhanced controllability. Specifically, we ask whether a short pulse of classifier-free guidance has a stronger effect when applied near the empirically identified critical scale than when applied at a random point along the denoising trajectory.

H.1 Model and sampling framework

We use a pretrained pixel-space EDM2 diffusion model on ImageNet at resolution 64×64 . The reverse dynamics are parameterized by the EDM noise variable σ , rather than by the variance-preserving time variable t used in the analytic patch model.

The deterministic reverse flow is written as

$$\frac{dx}{d\sigma} = b_\sigma(x, \sigma), \quad b_\sigma(x, \sigma) = \frac{x - D_\theta(x, \sigma, y)}{\sigma},$$

where $D_\theta(x, \sigma, y)$ denotes the class-conditional denoiser and y is the class label.

In the autoguided EDM2 setup, we also have an unconditional guide model $D_u(x, \sigma)$. This allows us to define a classifier-free guidance-type denoiser

$$D_{\text{cfg}}(x, \sigma, y; w) = D_\theta(x, \sigma, y) + w \left(D_\theta(x, \sigma, y) - D_u(x, \sigma) \right),$$

where w is the guidance scale.

The corresponding reverse drift under guidance is therefore

$$b_\sigma^{(w)}(x, \sigma) = \frac{x - D_{\text{cfg}}(x, \sigma, y; w)}{\sigma}.$$

Sampling is performed using the standard EDM sampler with Heun correction, with noise levels evolving from

$$\sigma_{\text{max}} = 80$$

to

$$\sigma_{\min} = 0.002.$$

The noise schedule is

$$\sigma_i = \left(\sigma_{\max}^{1/\rho} + \frac{i}{N-1} \left(\sigma_{\min}^{1/\rho} - \sigma_{\max}^{1/\rho} \right) \right)^\rho$$

with

$$\rho = 7.$$

H.2 Continuous-field dynamical analysis

To identify the critical regime of the reverse diffusion dynamics, we performed the same analysis used earlier for the EDM2 trajectories.

Continuous correlation length. Because the EDM2 model generates natural RGB images, a sign-binarized estimator is inappropriate. Instead, each image is first converted to luminance

$$\ell(x) = 0.2989 R + 0.5870 G + 0.1140 B,$$

and centered by subtracting the spatial mean:

$$\tilde{\ell}(x) = \ell(x) - \langle \ell(x) \rangle.$$

The connected spatial correlation function is computed as

$$C(r; \sigma) = \langle \tilde{\ell}(x) \tilde{\ell}(x+r) \rangle.$$

The spatial correlation length is then estimated using a second-moment estimator,

$$\xi_x(\sigma) = \sqrt{\frac{\sum_r r^2 C(r; \sigma)}{\sum_r C(r; \sigma)}}.$$

Linearized drift and low-frequency modes. To probe the stability of the reverse dynamics, we computed directional derivatives of the Jacobian of the unguided reverse drift,

$$J_\sigma(x) = \frac{\partial b_\sigma(x, \sigma)}{\partial x},$$

along Fourier modes

$$v_{n,x}(i, j) = \cos(nk_{\min} i), \quad v_{n,y}(i, j) = \cos(nk_{\min} j),$$

with

$$k_{\min} = \frac{2\pi}{L}.$$

For a direction v , the directional derivative was estimated using finite differences:

$$\lambda_v(\sigma) = \frac{v^\top [b_\sigma(x + \varepsilon v, \sigma) - b_\sigma(x - \varepsilon v, \sigma)]}{2\varepsilon}.$$

To stabilize the estimate, the finite-difference step was scaled with σ .

Equilibrium correlation length proxy. Following the same logic as in the patch model, we estimated an equilibrium correlation length from the normalized low-frequency dispersion of the Jacobian. Let $\lambda_n(\sigma)$ denote the shell-averaged low-frequency directional derivative. We fit

$$\frac{\lambda_n(\sigma)}{\lambda_0(\sigma)} \approx 1 + \xi_{\text{eq}}(\sigma)^2 (nk_{\min})^2.$$

This normalization removes the rapidly increasing overall stiffness of the drift at small σ and isolates the spatial curvature of the spectrum. The resulting quantity $\xi_{\text{eq}}(\sigma)$ serves as a proxy for the equilibrium correlation length of fluctuations around the instantaneous denoising branch.

H.3 Global critical scale estimation

A naive strategy would be to estimate a separate critical scale for each class. In practice, however, this estimate is noisy because the Jacobian-based equilibrium-length proxy is sensitive to finite-sample fluctuations.

To reduce variance, we used a global procedure. We first generated unguided trajectories for all selected classes and computed $\xi_{\text{eq}}(\sigma)$ for each trajectory. These curves were then aggregated across all classes and trajectories, and a single global critical scale was defined as

$$\sigma_c = \arg \max_{\sigma} \text{median } \xi_{\text{eq}}(\sigma).$$

This construction has two advantages:

- it suppresses class-specific noise in the equilibrium-length estimate,
- it identifies a single intervention scale that can be applied uniformly across classes.

Operationally, σ_c marks the window in which the low-frequency modes of the reverse drift are globally the softest.

H.4 Pulse-guidance intervention

After estimating the global critical scale, we ran two intervention conditions.

Critical-pulse condition. A guidance pulse of strength w_{pulse} was applied only within a short interval centered at the global critical scale:

$$w(\sigma) = \begin{cases} w_{\text{pulse}}, & \sigma \in [\sigma_c - \Delta, \sigma_c + \Delta], \\ 0, & \text{otherwise.} \end{cases}$$

Random-pulse condition. A pulse of identical strength and width was applied, but with center sampled uniformly at random in σ :

$$\sigma_{\text{rand}} \sim \text{Unif}[\sigma_{\text{min}}, \sigma_{\text{max}}],$$

and

$$w(\sigma) = \begin{cases} w_{\text{pulse}}, & \sigma \in [\sigma_{\text{rand}} - \Delta, \sigma_{\text{rand}} + \Delta], \\ 0, & \text{otherwise.} \end{cases}$$

Thus the only difference between the two conditions is the location of the pulse along the reverse trajectory.

H.5 Classes, trials, and hyperparameters

We selected 10 ImageNet classes and generated 40 samples per class and per condition.

The pulse experiment therefore consisted of

$$10 \text{ classes} \times 2 \text{ conditions} \times 40 \text{ trials}$$

for a total of 800 guided generations.

The key hyperparameters were:

Number of classes	10
Trials per class per condition	40
Critical scale	global, estimated from all classes
Pulse width	2Δ in σ
Pulse strength	fixed strong guidance scale
Conditions	critical pulse / random pulse

H.6 Class-alignment metric

To quantify whether the pulse improved semantic targeting, final generated images were evaluated with a pretrained DINOv2 ImageNet classifier.

For a generated image x , the classifier produces logits $z_c(x)$ and probabilities

$$p_c(x) = \frac{e^{z_c(x)}}{\sum_{c'} e^{z_{c'}(x)}}.$$

For a target class y , we recorded:

- the target-class logit $z_y(x)$,
- the target-class probability $p_y(x)$,
- whether the top predicted class matched the target class.

These quantities were averaged across trials for each class and condition.

H.7 Statistical comparison

For each class, we compared the critical-pulse and random-pulse conditions using the mean target probability, mean target logit, and top-1 correctness fraction. We report per-class summary tables of the form

$$\begin{aligned}\Delta p_y &= \bar{p}_y^{\text{critical}} - \bar{p}_y^{\text{random}}, \\ \Delta z_y &= \bar{z}_y^{\text{critical}} - \bar{z}_y^{\text{random}}.\end{aligned}$$

Positive values indicate that the pulse delivered near the critical scale yields better class alignment than a pulse delivered at a random point.

H.8 Interpretation

The theoretical picture developed in the main text predicts that the reverse diffusion dynamics pass through a critical window in which long-wavelength modes are especially soft. In that regime, perturbations to the drift should have disproportionate influence on the macroscopic organization of the sample.

The pulse-guidance experiment tests this directly. If the critical-scale pulse outperforms the random pulse, this indicates that the identified soft-mode regime is not merely a descriptive signature of generation dynamics, but a stage at which the model is maximally susceptible to semantically structured control.

The observed improvement in class alignment under critical-time pulses supports exactly this interpretation. It shows that the critical regime is an operationally meaningful feature of the reverse diffusion process and can be exploited to intervene on generation more efficiently than by applying the same guidance signal at an arbitrary point in the denoising trajectory.

H.9 Visualization of guided and unguided trajectories

To complement the quantitative metrics, we also visualized denoising trajectories under unguided sampling and under critical-pulse sampling. For a fixed class and random seed, we plotted a sequence of intermediate denoising states across 10 logarithmically spaced values of σ .

These visualizations illustrate how the pulse intervention changes the trajectory specifically near the critical regime, while leaving the remainder of the reverse process unchanged. This makes it possible to isolate the dynamical leverage of the critical window directly at the level of the image trajectory.

I Additional results

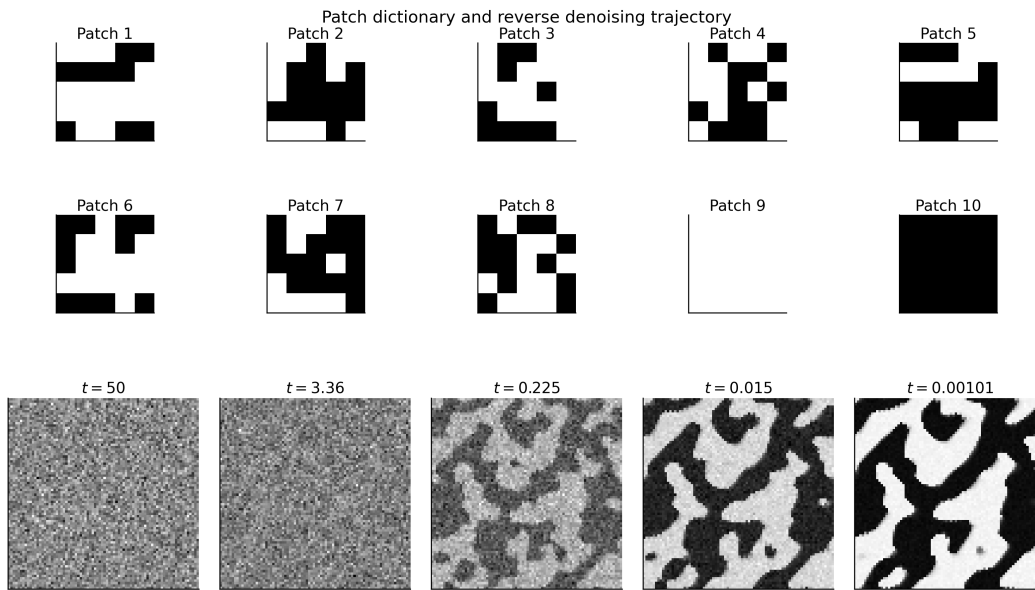


Figure 5: Patch dictionary (top) and a representative reverse denoising trajectory (bottom). Five snapshots of the evolving configuration are shown at logarithmically spaced times along the reverse diffusion path. Initially the field is dominated by noise, while at later times large coherent domains form as the dynamics selects one of the dominant global patterns.

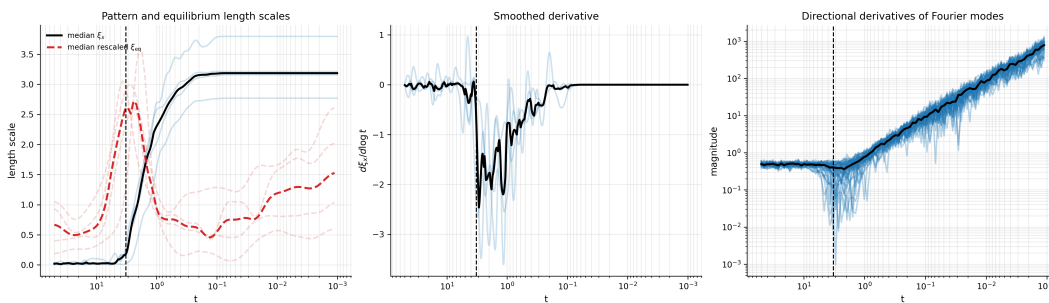


Figure 6: Quantitative analysis of pattern formation dynamics on binarized ConvNets trained on FashionMNIST.

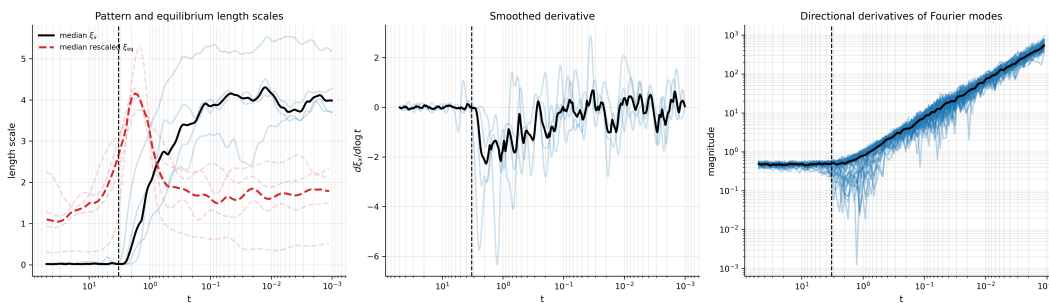


Figure 7: Quantitative analysis of pattern formation dynamics on non-binarized ConvNets trained on FashionMNIST. The critical line is estimated under the (incorrect) binary theory, so it should be interpreted as a rough estimate.